



Differential branching fraction and angular moments analysis of the decay $B^0 \rightarrow K^+ \pi^- \mu^+ \mu^-$ in the $K_{0,2}^*(1430)^0$ region

The LHCb collaboration[†]

Abstract

Measurements of the differential branching fraction and angular moments of the decay $B^0 \rightarrow K^+ \pi^- \mu^+ \mu^-$ in the $K^+ \pi^-$ invariant mass range $1330 < m(K^+ \pi^-) < 1530$ MeV/ c^2 are presented. Proton-proton collision data are used, corresponding to an integrated luminosity of 3 fb^{-1} collected by the LHCb experiment. Differential branching fraction measurements are reported in five bins of the invariant mass squared of the dimuon system, q^2 , between 0.1 and $8.0 \text{ GeV}^2/c^4$. For the first time, an angular analysis sensitive to the S-, P- and D-wave contributions of this rare decay is performed. The set of 40 normalised angular moments describing the decay is presented for the q^2 range 1.1–6.0 GeV^2/c^4 .

Published in JHEP **12** (2016) 065

© CERN on behalf of the LHCb collaboration, licence CC-BY-4.0.

[†]Authors are listed at the end of this paper.

1 Introduction

The decay $B^0 \rightarrow K^+\pi^-\mu^+\mu^-$ is a flavour-changing neutral-current process.¹ In the Standard Model (SM), the leading order transition amplitudes are described by electroweak penguin or box diagrams. In extensions to the SM, new heavy particles can contribute to loop diagrams and modify observables such as branching fractions and angular distributions.

The previous angular analyses of $B^0 \rightarrow K^+\pi^-\mu^+\mu^-$ performed by the LHCb collaboration [1–4] focused on the $K^+\pi^-$ invariant mass range $796 < m(K^+\pi^-) < 996 \text{ MeV}/c^2$ where the decay proceeds predominantly via the P-wave process $K^*(892)^0 \rightarrow K^+\pi^-$. A global analysis of the CP -averaged angular observables measured in the LHCb Run 1 data sample indicated differences from SM predictions at the level of 3.4 standard deviations [4]. This measurement is widely discussed in the literature (see, for instance, [5–8] and references therein). It is still not clear if this discrepancy could be caused by an underestimation of the theory uncertainty on hadronic effects or if it requires a New Physics explanation. Since short-distance effects should be universal in all $b \rightarrow s\mu\mu$ transitions, measuring other such transitions can shed light on this situation. Recently, the S-wave contribution to $B^0 \rightarrow K^+\pi^-\mu^+\mu^-$ decays has been measured in the $644 < m(K^+\pi^-) < 1200 \text{ MeV}/c^2$ region [9].

Since the dominant structures in the $K^+\pi^-$ invariant mass spectrum of $B^0 \rightarrow K^+\pi^-\mu^+\mu^-$ above the P-wave $K^*(892)^0$ are resonances in the $1430 \text{ MeV}/c^2$ region, this is a natural region to study. The relevant K^{*0} states above the $K^*(892)^0$ mass range are listed in Table 1. Throughout this paper, the symbol K^{*0} denotes any neutral strange meson in an excited state that decays to a $K^+\pi^-$ final state. In the $1430 \text{ MeV}/c^2$ region, contributions are expected from the S-wave $K_0^*(1430)^0$, P-wave $K^*(1410)^0$ and D-wave $K_2^*(1430)^0$ states, as well as the broad P-wave $K^*(1680)^0$ state. The mass region of the higher K_J^* resonances was studied in Ref. [11] with model-dependent theoretical predictions based on QCD form-factors. However, since the form-factors for broad resonances remain poorly known, a more model-independent prescription was provided in Ref. [12], which is used in this analysis.

The $m(K^+\pi^-)$ distribution for $B^0 \rightarrow K^+\pi^-\mu^+\mu^-$ decays in the range $1.1 < q^2 < 6.0 \text{ GeV}^2/c^4$ and $630 < m(K^+\pi^-) < 1630 \text{ MeV}/c^2$ is shown in Fig. 1, where $q^2 \equiv m^2(\mu^+\mu^-)$. The candidates are obtained using the selection described in Sec. 4 and the background component is subtracted using the *sPlot* technique [13]. The main structures are observed

¹The inclusion of charge conjugate processes is implied, unless otherwise noted.

Table 1: Expected resonant contributions above the $K^*(892)^0$ mass range. For each, the spin-parity, J^P , and branching fraction to $K\pi$, $\mathcal{B}(K\pi)$, are given (taken from Ref. [10]).

Resonance	J^P	Mass [MeV/c^2]	Full width [MeV/c^2]	$\mathcal{B}(K\pi)$ [%]
$K^*(1410)^0$	1^-	1414 ± 15	232 ± 21	6.6 ± 1.3
$K_0^*(1430)^0$	0^+	1425 ± 50	270 ± 80	93 ± 10
$K_2^*(1430)^0$	2^+	1432.4 ± 1.3	109 ± 5	49.9 ± 1.2
$K^*(1680)^0$	1^-	1717 ± 27	322 ± 110	38.7 ± 2.5
$K_3^*(1780)^0$	3^-	1776 ± 7	159 ± 21	18.8 ± 1.0
$K_4^*(2045)^0$	4^+	2045 ± 9	198 ± 30	9.9 ± 1.2

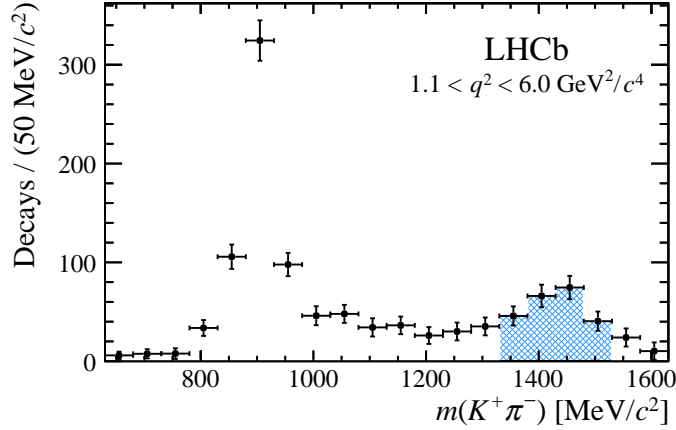


Figure 1: Background-subtracted $m(K^+\pi^-)$ distribution for $B^0 \rightarrow K^+\pi^-\mu^+\mu^-$ decays in the range $1.1 < q^2 < 6.0 \text{ GeV}^2/c^4$. The region $1330 < m(K^+\pi^-) < 1530 \text{ MeV}/c^2$ is indicated by the blue, hatched area.

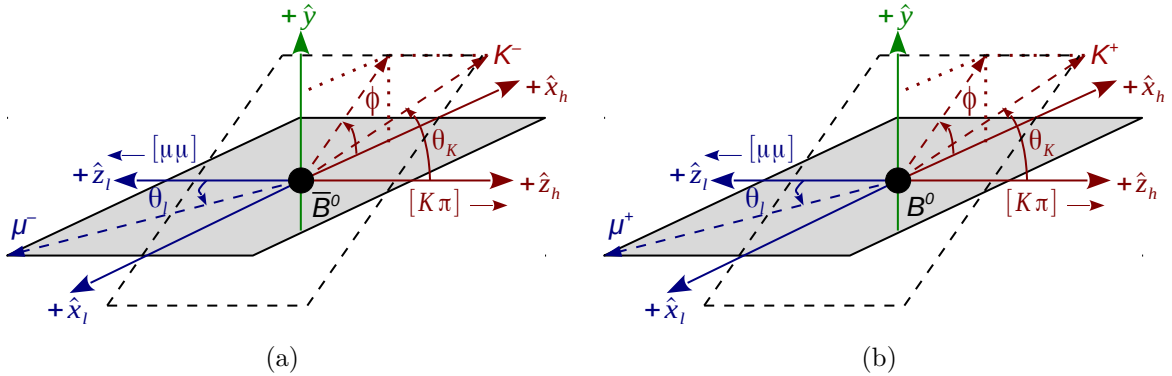


Figure 2: Angle conventions for (a) $\bar{B}^0 \rightarrow K^-\pi^+\mu^+\mu^-$ and (b) $B^0 \rightarrow K^+\pi^-\mu^+\mu^-$, as described in Ref. [12]. The leptonic and hadronic frames are back-to-back with a common \hat{y} axis. For the dihedral angle ϕ between the leptonic and hadronic decay planes, there is an additional sign flip $\phi \rightarrow -\phi$ compared to previous LHCb analyses [1–4].

around the mass of the $K^*(892)^0$ resonance and in the $1430 \text{ MeV}/c^2$ region.

This paper presents the first measurements of the differential branching fraction and angular moments of $B^0 \rightarrow K^+\pi^-\mu^+\mu^-$ in the region $1330 < m(K^+\pi^-) < 1530 \text{ MeV}/c^2$. The values of the differential branching fraction are reported in five bins of q^2 between 0.1 and $8.0 \text{ GeV}^2/c^4$, and in the range $1.1 < q^2 < 6.0 \text{ GeV}^2/c^4$ for which the angular moments are also measured. The measurements are based on samples of pp collisions collected by the LHCb experiment in Run 1, corresponding to integrated luminosities of 1.0 fb^{-1} at a centre-of-mass energy of 7 TeV and 2.0 fb^{-1} at 8 TeV .

2 Angular distribution

The final state of the decay $B^0 \rightarrow K^+\pi^-\mu^+\mu^-$ is fully described by five kinematic variables: three decay angles (θ_ℓ , θ_K , ϕ), $m(K^+\pi^-)$, and q^2 . Figure 2a shows the angle conventions

for the \bar{B}^0 decay (containing a b quark): the back-to-back leptonic and hadronic systems share a common \hat{y} axis and have opposite \hat{x} and \hat{z} axes. The negatively charged lepton is used to define the leptonic helicity angle θ_ℓ for the \bar{B}^0 . The quadrant of the dihedral angle ϕ between the dimuon and the $\bar{K}^{*0} \rightarrow K^-\pi^+$ decay planes is determined by requiring the azimuthal angle of the μ^- to be zero in the leptonic helicity frame. The azimuthal angle of the K^- in the hadronic helicity frame is then equal to ϕ . Compared to the dihedral angle used in the previous LHCb analyses [1–4], there is a sign flip, $\phi \rightarrow -\phi$, in the convention used here. For the B^0 decay (containing a \bar{b} quark), the charge conjugation is performed explicitly, and the angles are shown in Fig. 2b, where for the B^0 , the μ^+ and K^+ directions are used to define the angles. An additional minus sign is added to the dihedral angle when performing the CP conjugation, in order to keep the measured angular observables the same between \bar{B}^0 and B^0 in the absence of direct CP violation.

In the limit where q^2 is large compared to the square of the muon mass, the CP -averaged differential decay rate of $B^0 \rightarrow K^+\pi^-\mu^+\mu^-$ with the $K^+\pi^-$ system in a S-, P-, or D-wave configuration can be expanded in an orthonormal basis of angular functions $f_i(\Omega)$ as

$$\frac{d\Gamma}{dq^2 d\Omega} \propto \sum_{i=1}^{41} f_i(\Omega) \Gamma_i(q^2) \quad \text{with} \quad \Gamma_i(q^2) = \Gamma_i^L(q^2) + \eta_i^{L \rightarrow R} \Gamma_i^R(q^2), \quad (1)$$

where $d\Omega = d\cos\theta_\ell d\cos\theta_K d\phi$, and L and R denote the (left- and right-handed) chirality of the lepton system [12]. The sign $\eta_i^{L \rightarrow R} = \pm 1$ depends on whether f_i changes sign under $\theta_\ell \rightarrow \pi + \theta_\ell$. The orthonormal angular basis is constructed out of spherical harmonics, $Y_l^m \equiv Y_l^m(\theta_\ell, \phi)$, and reduced spherical harmonics, $P_l^m \equiv \sqrt{2\pi} Y_l^m(\theta_K, 0)$.

The transversity-basis moments of the 41 orthonormal angular functions are given in Appendix A. The convention is that the amplitudes correspond to the \bar{B}^0 decay, with the corresponding amplitudes for the B^0 decay obtained by flipping the signs of the helicities and weak phases. The S-, P- and D-wave transversity amplitudes are denoted as $S^{\{L,R\}}$, $H_{\{0,\parallel,\perp\}}^{\{L,R\}}$ and $D_{\{0,\parallel,\perp\}}^{\{L,R\}}$, respectively.

The measured angular observables are averaged over the range $1330 < m(K^+\pi^-) < 1530$ MeV/ c^2 and $1.1 < q^2 < 6.0$ GeV $^2/c^4$. This q^2 range is part of the large-recoil regime where the recoiling K^{*0} has a relatively large energy, $E_{K^{*0}}$, as measured in the rest frame of the parent B meson. In the limit $\Lambda_{\text{QCD}}/E_{K^{*0}} \rightarrow 0$, the uncertainties arising from hadronic effects in the relevant form-factors are reduced at leading order, resulting in more reliable theory predictions [5]. The high- q^2 region above the $\psi(2S)$ resonance is polluted by broad charmonium resonances and is also phase-space suppressed for higher $m(K^+\pi^-)$ masses. Therefore, that region is not considered in this study.

In the present analysis, the first moment, $\Gamma_1(q^2)$, corresponds to the total decay rate. From this, 40 normalised moments for $i \in \{2, \dots, 41\}$ are defined as

$$\bar{\Gamma}_i(q^2) = \frac{\Gamma_i(q^2)}{\Gamma_1(q^2)}. \quad (2)$$

These form the set of observables that are measured in the angular moments analysis described in Sec. 8.

3 Detector and simulation

The LHCb detector [14, 15] is a single-arm forward spectrometer covering the pseudorapidity range $2 < \eta < 5$, designed for the study of particles containing b or c quarks. The detector includes a high-precision tracking system consisting of a silicon-strip vertex detector surrounding the pp interaction region, a large-area silicon-strip detector located upstream of a dipole magnet with a bending power of about 4 Tm, and three stations of silicon-strip detectors and straw drift tubes placed downstream of the magnet. The tracking system provides a measurement of momentum of charged particles with a relative uncertainty that varies from 0.5% at low momentum to 1.0% at 200 GeV/ c . The minimum distance of a track to a primary vertex (PV), the impact parameter (IP), is measured with a resolution of $(15 + 29/p_T) \mu\text{m}$, where p_T is the component of the momentum transverse to the beam, in GeV/ c . Different types of charged hadrons are distinguished using information from two ring-imaging Cherenkov detectors. Photons, electrons and hadrons are identified by a calorimeter system consisting of scintillating-pad and preshower detectors, an electromagnetic calorimeter and a hadronic calorimeter. Muons are identified by a system composed of alternating layers of iron and multiwire proportional chambers. The online event selection is performed by a trigger, which consists of a hardware stage, based on information from the calorimeter and muon systems, followed by a software stage, which applies a full event reconstruction.

Simulated signal events are used to determine the effect of the detector geometry, trigger, reconstruction and selection on the angular distributions of the signal and of the $B^0 \rightarrow J/\psi K^*(892)^0$ mode, which is used for normalisation. Additional simulated samples are used to estimate the contribution from specific background processes. In the simulation, pp collisions are generated using PYTHIA [16, 17] with a specific LHCb configuration [18]. Decays of hadronic particles are described by EVTGEN [19], in which final-state radiation is generated using PHOTOS [20]. The interaction of the generated particles with the detector, and its response, are implemented using the GEANT4 toolkit [21] as described in Ref. [22]. Data-driven techniques are used to correct the simulation for mismodelling of the detector occupancy, the B^0 meson momentum and vertex quality distributions, and particle identification performance.

4 Selection of signal candidates

The $B^0 \rightarrow K^+ \pi^- \mu^+ \mu^-$ signal candidates are first required to pass the hardware trigger, which selects events containing at least one muon with transverse momentum $p_T > 1.48 \text{ GeV}/c$ in the 7 TeV data or $p_T > 1.76 \text{ GeV}/c$ in the 8 TeV data. In the subsequent software trigger, at least one of the final-state particles is required to have both $p_T > 1.0 \text{ GeV}/c$ and an impact parameter larger than $100 \mu\text{m}$ with respect to all PVs in the event. Finally, the tracks of two or more of the final-state particles are required to form a vertex significantly displaced from all PVs.

Signal candidates are formed from a pair of oppositely charged tracks identified as muons, combined with two oppositely charged tracks identified as a kaon and a pion. These signal candidates are then required to pass a set of loose preselection requirements, identical to those described in Ref. [4] with the exception that the $K^+ \pi^-$ system is permitted to be in the wider mass range $630 < m(K^+ \pi^-) < 1630 \text{ MeV}/c^2$. This allows the decay $B^0 \rightarrow$

$J/\psi K^*(892)^0$ to be used as a normalisation mode for the branching fraction measurement. Candidates are required to have good quality vertex and track fits, and a reconstructed B^0 invariant mass in the range $5170 < m(K^+\pi^-\mu^+\mu^-) < 5700 \text{ MeV}/c^2$. From this point onwards, the normalisation mode is selected in the range $796 < m(K^+\pi^-) < 996 \text{ MeV}/c^2$ and the signal in the range $1330 < m(K^+\pi^-) < 1530 \text{ MeV}/c^2$.

The backgrounds from combining unrelated particles, mainly from different b and c hadron decays, are referred to as combinatorial. Such backgrounds are suppressed with the use of a Boosted Decision Tree (BDT) [23,24]. The BDT used for the present analysis is identical to that described in Ref. [4] and the same working point is used.

Exclusive background processes can mimic the signal if their final states are misidentified or misreconstructed. For the present analysis, the requirements of Ref. [4] for the $K^*(892)^0$ region are applied to a wider $m(K^+\pi^-)$ invariant mass window. However, to reduce the expected contamination from peaking background to the level of 2% of the signal yield, it is necessary to modify two of them. First, the requirement to remove contributions from $B^0 \rightarrow J/\psi K^*(892)^0$ candidates, where the π^- (K^+) is misidentified as a μ^- (μ^+) and the μ^- (μ^+) is misidentified as a π^- (K^+), is tightened by extending the invariant mass window of the $\mu^+\pi^-$ ($K^+\mu^-$) system and requiring stricter muon identification criteria. Second, the requirement to remove the contributions from genuine $B^0 \rightarrow K^+\pi^-\mu^+\mu^-$ decays where the two hadron hypotheses are interchanged is tightened by requiring stricter hadron identification criteria.

5 Acceptance correction

The triggering, reconstruction and selection of candidates distorts their kinematic distributions. The dominant acceptance effects are due to the requirements on track momentum and impact parameter.

The method for obtaining the acceptance correction, described in Ref. [4], is extended to include the $m(K^+\pi^-)$ dimension. The efficiency is parameterised in terms of Legendre polynomials of order n , $L_n(x)$, as

$$\varepsilon(q^{2'}, \cos \theta_\ell, \cos \theta_K, \phi', m'(K^+\pi^-)) = \sum_{hijkl} c_{hijkl} L_h(q^{2'}) L_i(\cos \theta_\ell) L_j(\cos \theta_K) L_k(\phi') L_l(m'(K^+\pi^-)). \quad (3)$$

As the polynomials are defined over the domain $x \in [-1, 1]$, the variables $q^{2'}$, ϕ' and $m'(K^+\pi^-)$ are used, which are obtained by linearly transforming q^2 , ϕ and $m(K^+\pi^-)$ to lie in this range. The sum in Eq. 3 encompasses $L_n(x)$ up to fourth order in $\cos \theta_\ell$ and $m'(K^+\pi^-)$, sixth order in ϕ' and $q^{2'}$, and eighth order in $\cos \theta_K$. The coefficients c_{hijkl} are determined using a moment analysis of simulated $B^0 \rightarrow K^+\pi^-\mu^+\mu^-$ decays, generated according to a phase space distribution. The angular acceptance as a function of $\cos \theta_\ell$, $\cos \theta_K$ and ϕ' in the region $1.1 < q^2 < 6.0 \text{ GeV}^2/c^4$ and $1330 < m(K^+\pi^-) < 1530 \text{ MeV}/c^2$ is shown in Fig. 3.

6 The $m(K^+\pi^-\mu^+\mu^-)$ invariant mass distribution

The invariant mass $m(K^+\pi^-\mu^+\mu^-)$ is used to discriminate between signal and background. The signal distribution is modelled as the sum of two Gaussian functions with a common

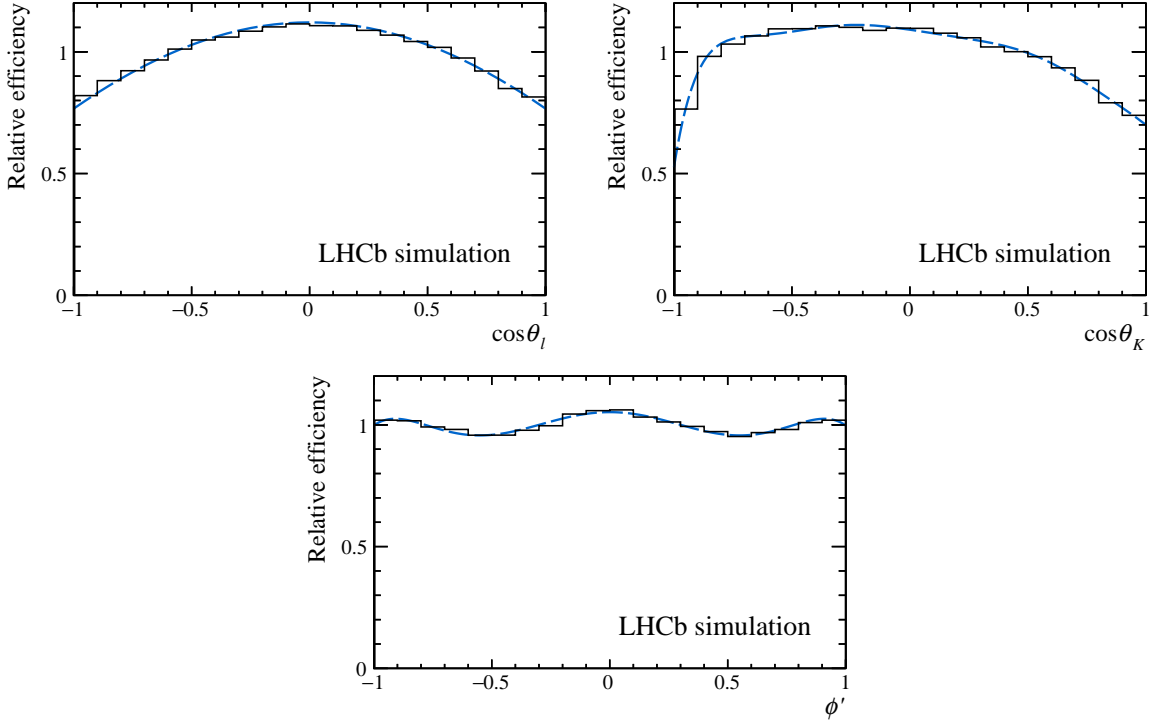


Figure 3: Relative efficiency in $\cos\theta_\ell$, $\cos\theta_K$ and ϕ' in the region $1.1 < q^2 < 6.0 \text{ GeV}^2/c^4$ and $1330 < m(K^+\pi^-) < 1530 \text{ MeV}/c^2$ as determined from a moment analysis of simulated $B^0 \rightarrow K^+\pi^-\mu^+\mu^-$ decays, shown as a histogram. The efficiency function is shown by the blue, dashed line.

mean, each with a power-law tail on the low-mass side. The parameters describing the shape of the mass distribution of the signal are determined from a fit to the $B^0 \rightarrow J/\psi K^*(892)^0$ control mode, as shown in Fig. 4, and are subsequently fixed when fitting the $B^0 \rightarrow K^+\pi^-\mu^+\mu^-$ candidates. An additional component is included in the fit to the control mode to model the contribution from $B_s^0 \rightarrow J/\psi \bar{K}^{*0}$ decays. A single scaling factor is used to correct the width of the Gaussian functions to account for variations in the shape of the mass distribution of the signal observed in simulation, due to the different regions of $m(K^+\pi^-)$ and q^2 between the control mode and signal mode. The combinatorial background is modelled using an exponential function. The fit to $B^0 \rightarrow K^+\pi^-\mu^+\mu^-$ candidates in the range $1.1 < q^2 < 6.0 \text{ GeV}^2/c^4$ is shown in Fig. 4. The signal yield in the range $1.1 < q^2 < 6.0 \text{ GeV}^2/c^4$ is 229 ± 21 . The fits to $B^0 \rightarrow K^+\pi^-\mu^+\mu^-$ candidates in each of the q^2 bins used for the differential branching fraction measurement are shown in Appendix B.

7 Differential branching fraction

The differential branching fraction $d\mathcal{B}/dq^2$ of the decay $B^0 \rightarrow K^+\pi^-\mu^+\mu^-$ in an interval (q_{\min}^2, q_{\max}^2) is given by

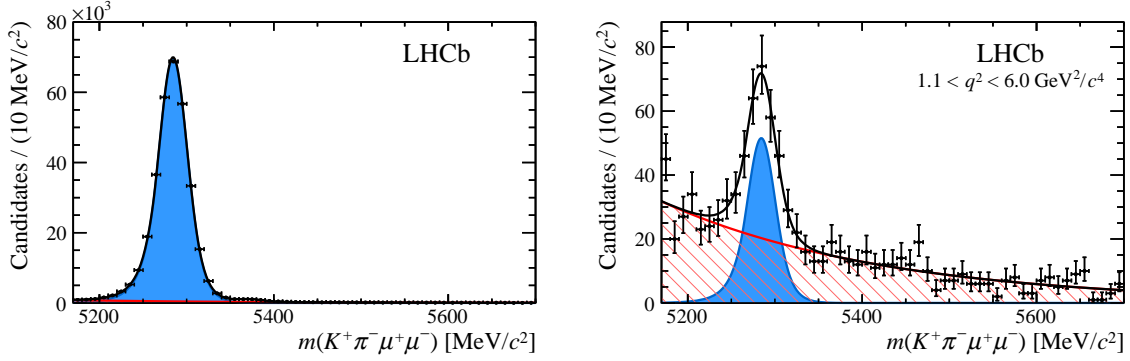


Figure 4: Invariant mass $m(K^+\pi^-\mu^+\mu^-)$ for (left) the control decay $B^0 \rightarrow J/\psi K^{*0}$ and (right) the signal decay $B^0 \rightarrow K^+\pi^-\mu^+\mu^-$ in the bin $1.1 < q^2 < 6.0 \text{ GeV}^2/c^4$. The solid black line represents the total fitted function. The individual components of the signal (blue, shaded area) and combinatorial background (red, hatched area) are also shown.

$$\frac{d\mathcal{B}}{dq^2} = \frac{1}{(q_{\text{max}}^2 - q_{\text{min}}^2)} f_{K^*(892)^0} \mathcal{B}(B^0 \rightarrow J/\psi K^*(892)^0) \mathcal{B}(J/\psi \rightarrow \mu^+\mu^-) \times \mathcal{B}(K^*(892)^0 \rightarrow K^+\pi^-) \frac{N'_{K^+\pi^-\mu^+\mu^-}}{(1 - F_S^{J/\psi K^*0}) N'_{J/\psi K^*0}}, \quad (4)$$

where $N'_{K^+\pi^-\mu^+\mu^-}$ and $N'_{J/\psi K^*0}$ are the acceptance-corrected yields of the $B^0 \rightarrow K^+\pi^-\mu^+\mu^-$ and $B^0 \rightarrow J/\psi (\rightarrow \mu^+\mu^-) K^*0 (\rightarrow K^+\pi^-)$ decays, respectively. The $B^0 \rightarrow J/\psi K^*0$ yield has to be corrected for the S-wave fraction within the $796 < m(K^+\pi^-) < 996 \text{ MeV}/c^2$ window of $B^0 \rightarrow J/\psi K^*0$ decays, $F_S^{J/\psi K^*0}$. The value of $F_S^{J/\psi K^*0} = 0.084 \pm 0.01$ is obtained from Ref. [25], after recalculation for the $m(K^+\pi^-)$ range $796 < m(K^+\pi^-) < 996 \text{ MeV}/c^2$. The branching fractions $\mathcal{B}(B^0 \rightarrow J/\psi K^*(892)^0)$, $\mathcal{B}(J/\psi \rightarrow \mu^+\mu^-)$ and $\mathcal{B}(K^*(892)^0 \rightarrow K^+\pi^-)$ are $(1.19 \pm 0.01 \pm 0.08) \times 10^{-3}$ [26], $(5.961 \pm 0.033) \times 10^{-2}$ [10] and $2/3$, respectively. The fraction $f_{K^*(892)^0}$ is used to scale the value of $\mathcal{B}(B^0 \rightarrow J/\psi K^*(892)^0)$ to the appropriate $m(K^+\pi^-)$ range and is calculated by integrating the $K^*(892)^0$ line shape given in Ref. [26] over the range $796 < m(K^+\pi^-) < 996 \text{ MeV}/c^2$.

In order to obtain the acceptance-corrected yield, the efficiency function described in Sec. 5 is used to evaluate an acceptance weight for each candidate. An average acceptance weight is determined for both the $B^0 \rightarrow J/\psi K^*0$ candidates and the signal candidates in each q^2 bin. The acceptance-corrected yield is then equal to the measured yield multiplied by the average weight. The average weight is calculated within the $\pm 50 \text{ MeV}/c^2$ signal window around the mean B^0 mass and also in the background region taken from the upper mass sideband in the range $5350 < m(K^+\pi^-\mu^+\mu^-) < 5700 \text{ MeV}/c^2$. The latter is subsequently used to subtract the background contribution from the average weight obtained in the $\pm 50 \text{ MeV}/c^2$ window, taking into account the extrapolated background yield in this window. This method avoids making any assumption about the unknown angular distribution of the $B^0 \rightarrow K^+\pi^-\mu^+\mu^-$ decay.

The results for the differential branching fraction are given in Fig. 5. The uncertainties shown are the sums in quadrature of the statistical and systematic uncertainties. The results are also presented in Table 2. The various sources of the systematic uncertainties are described in Sec. 9.

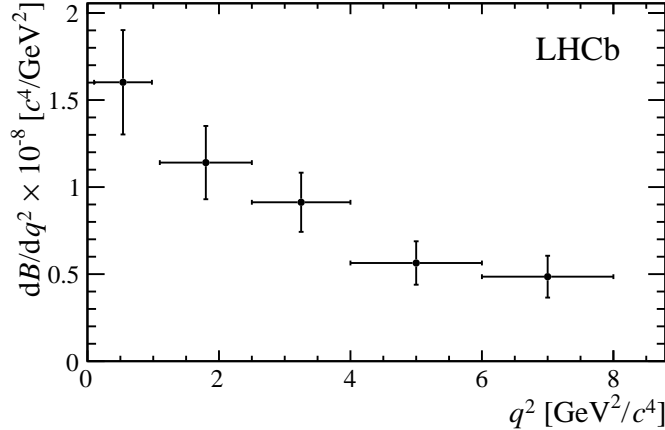


Figure 5: Differential branching fraction of $B^0 \rightarrow K^+\pi^-\mu^+\mu^-$ in bins of q^2 for the range $1330 < m(K^+\pi^-) < 1530 \text{ MeV}/c^2$. The error bars indicate the sums in quadrature of the statistical and systematic uncertainties.

Table 2: Differential branching fraction of $B^0 \rightarrow K^+\pi^-\mu^+\mu^-$ in bins of q^2 for the range $1330 < m(K^+\pi^-) < 1530 \text{ MeV}/c^2$. The first uncertainty is statistical, the second systematic and the third due to the uncertainty on the $B^0 \rightarrow J/\psi K^*(892)^0$ and $J/\psi \rightarrow \mu^+\mu^-$ branching fractions.

q^2 [GeV^2/c^4]	$d\mathcal{B}/dq^2 \times 10^{-8}$ [c^4/GeV^2]
[0.10, 0.98]	$1.60 \pm 0.28 \pm 0.04 \pm 0.11$
[1.10, 2.50]	$1.14 \pm 0.19 \pm 0.03 \pm 0.08$
[2.50, 4.00]	$0.91 \pm 0.16 \pm 0.03 \pm 0.06$
[4.00, 6.00]	$0.56 \pm 0.12 \pm 0.02 \pm 0.04$
[6.00, 8.00]	$0.49 \pm 0.11 \pm 0.01 \pm 0.03$
[1.10, 6.00]	$0.82 \pm 0.09 \pm 0.02 \pm 0.06$

8 Angular moments analysis

The angular observables defined in Sec. 2 are determined using a moments analysis of the angular distribution, as outlined in Ref. [12]. This approach has the advantage of producing stable measurements with well-defined uncertainties even for small data samples. Similar methods using angular moments are described in Refs. [27, 28].

The 41 background-subtracted and acceptance-corrected moments are estimated as

$$\Gamma_i = \sum_{k=1}^{n_{\text{sig}}} w_k f_i(\Omega_k) - x \sum_{k=1}^{n_{\text{bkg}}} w_k f_i(\Omega_k) \quad (5)$$

and the corresponding covariance matrix is estimated as

$$C_{ij} = \sum_{k=1}^{n_{\text{sig}}} w_k^2 f_i(\Omega_k) f_j(\Omega_k) + x^2 \sum_{k=1}^{n_{\text{bkg}}} w_k^2 f_i(\Omega_k) f_j(\Omega_k). \quad (6)$$

Here n_{sig} and n_{bkg} correspond to the candidates in the signal and background regions, respectively. The signal region is defined within $\pm 50 \text{ MeV}/c^2$ of the mean B^0 mass, and the background region in the range $5350 < m(K^+\pi^-\mu^+\mu^-) < 5700 \text{ MeV}/c^2$. The scale factor x is the ratio of the estimated number of background candidates in the signal region over the number of candidates in the background region and is used to normalise the background subtraction. It has been checked in data that the angular distribution of the background is independent of $m(K^+\pi^-\mu^+\mu^-)$ within the precision of this measurement, and that the uncertainty on x has negligible impact on the results. The weights, w_k , are the reciprocals of the candidates' efficiencies and account for the acceptance, described in Sec. 5.

The covariance matrix describing the statistical uncertainties on the 40 normalised moments is computed as

$$\bar{C}_{ij} = \left[C_{ij} + \frac{\Gamma_i \Gamma_j}{\Gamma_1^2} C_{11} - \frac{\Gamma_i C_{1j} + \Gamma_j C_{1i}}{\Gamma_1} \right] \frac{1}{\Gamma_1^2}, \quad i, j \in \{2, \dots, 41\}. \quad (7)$$

The results for the normalised moments, $\bar{\Gamma}_i$, are given in Fig. 6. The uncertainties shown are the sums in quadrature of the statistical and systematic uncertainties. The results are also presented in Table 3. The various sources of the systematic uncertainties are described in Sec. 9. The complete set of numerical values for the measured moments and the covariance matrix is provided in Ref. [29].

The distributions of each of the decay angles within the signal region are shown in Fig. 7. The estimated signal distribution is derived from the moments model by evaluating the sum in Eq. 1, which is found to provide a good representation of the data for each of the decay angles.

The D-wave fraction, F_{D} , is estimated from the moments $\bar{\Gamma}_5$ and $\bar{\Gamma}_{10}$ as

$$F_{\text{D}} = -\frac{7}{18} \left(2\bar{\Gamma}_5 + 5\sqrt{5}\bar{\Gamma}_{10} \right). \quad (8)$$

Naively, one would expect a large D-wave contribution in this region, as was seen in the amplitude analysis of $B^0 \rightarrow J/\psi K^+\pi^-$ [26]. However, in $B^0 \rightarrow K^+\pi^-\mu^+\mu^-$ no significant D-wave contribution is seen and, with the limited statistics currently available, it is only possible to set an upper limit of $F_{\text{D}} < 0.29$ at 95% confidence level using the approach in Ref. [30]. This might be an indication of a large breaking of QCD factorisation due to non-factorizable diagrams where additional gluons are exchanged between the $K^+\pi^-$ and the $c\bar{c}$, before the J/ψ decays into $\mu^+\mu^-$. For electroweak penguins, similar effects could occur due to charm loops [8]. Additionally, the values of the moments $\bar{\Gamma}_2$ and $\bar{\Gamma}_3$ imply the presence of large interference effects between the S- and P- or D-wave contributions.

9 Systematic uncertainties

The main sources of systematic uncertainty for the measurements of the differential branching fraction and angular moments are described in detail below and summarised in Table 4. They are significantly smaller than the statistical uncertainties.

The differential branching fraction and angular moments analysis share several common systematic effects: the statistical uncertainty on the acceptance function due to the size of the simulated sample from which it is determined, differences between data and the

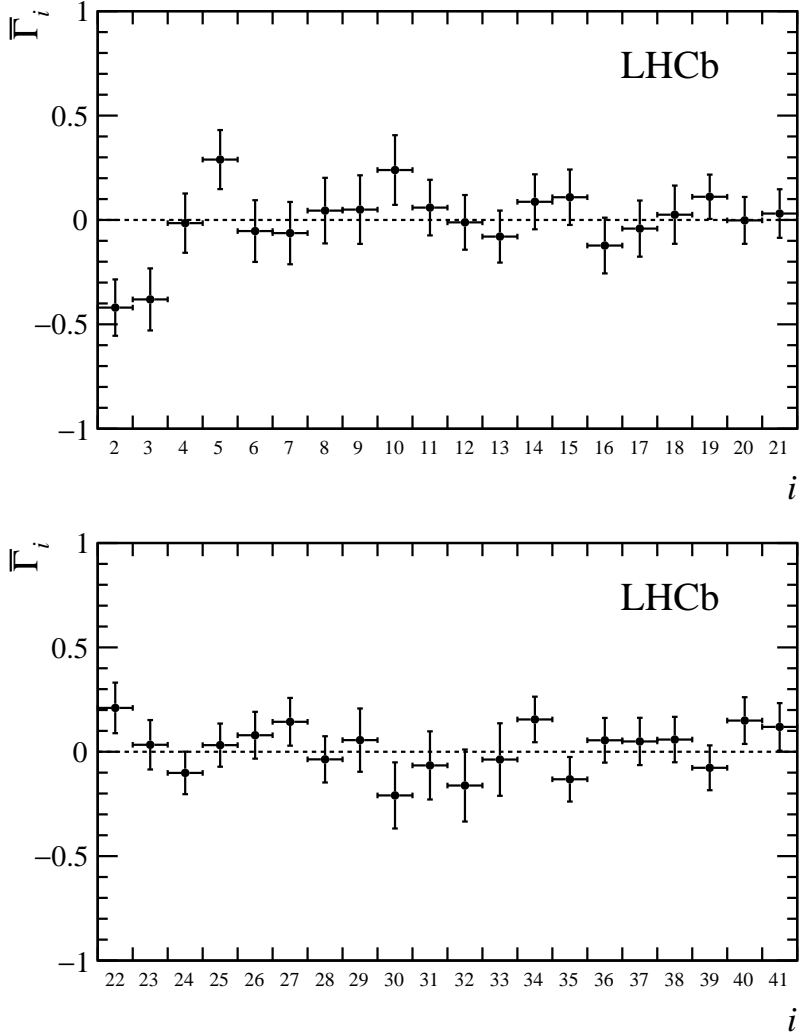


Figure 6: Measurement of the normalised moments, $\bar{\Gamma}_i$, of the decay $B^0 \rightarrow K^+ \pi^- \mu^+ \mu^-$ in the range $1.1 < q^2 < 6.0 \text{ GeV}^2/c^4$ and $1330 < m(K^+ \pi^-) < 1530 \text{ MeV}/c^2$. The error bars indicate the sums in quadrature of the statistical and systematic uncertainties.

simulated decays used to determine the acceptance function and contributions from residual peaking background candidates. The differential branching fraction has, in addition, a systematic uncertainty due to the uncertainty on the branching fraction of the decay $B^0 \rightarrow J/\psi K^*(892)^0$, which is dominant and is shown separately in Table 2.

The size of the systematic uncertainties associated with the determination of the acceptance correction and residual peaking background contributions are evaluated using pseudoexperiments, in which samples are generated varying one or more parameters. The differential branching fraction and each of the moments are evaluated using both the nominal model and the systematically varied models. In general, the systematic uncertainty is taken as the average of the difference between the nominal and varied models over a large number of pseudoexperiments. The exception to this is the statistical uncertainty of the acceptance function, due to the limited size of the simulated samples, for which the standard deviation is used instead. For this, pseudoexperiments are generated where the acceptance is varied according to the covariance matrix of the moments of the

Table 3: Measurement of the normalised moments, $\bar{\Gamma}_i$, of the decay $B^0 \rightarrow K^+\pi^-\mu^+\mu^-$ in the range $1.1 < q^2 < 6.0 \text{ GeV}^2/c^4$ and $1330 < m(K^+\pi^-) < 1530 \text{ MeV}/c^2$. The first uncertainty is statistical and the second systematic.

$\bar{\Gamma}_i$	Value	$\bar{\Gamma}_i$	Value
$\bar{\Gamma}_2$	$-0.42 \pm 0.13 \pm 0.03$	$\bar{\Gamma}_{22}$	$0.21 \pm 0.12 \pm 0.01$
$\bar{\Gamma}_3$	$-0.38 \pm 0.15 \pm 0.01$	$\bar{\Gamma}_{23}$	$0.03 \pm 0.12 \pm 0.01$
$\bar{\Gamma}_4$	$-0.02 \pm 0.14 \pm 0.01$	$\bar{\Gamma}_{24}$	$-0.10 \pm 0.10 \pm 0.01$
$\bar{\Gamma}_5$	$0.29 \pm 0.14 \pm 0.02$	$\bar{\Gamma}_{25}$	$0.03 \pm 0.10 \pm 0.01$
$\bar{\Gamma}_6$	$-0.05 \pm 0.14 \pm 0.04$	$\bar{\Gamma}_{26}$	$0.08 \pm 0.11 \pm 0.01$
$\bar{\Gamma}_7$	$-0.06 \pm 0.15 \pm 0.03$	$\bar{\Gamma}_{27}$	$0.14 \pm 0.11 \pm 0.01$
$\bar{\Gamma}_8$	$0.04 \pm 0.16 \pm 0.01$	$\bar{\Gamma}_{28}$	$-0.04 \pm 0.11 \pm 0.01$
$\bar{\Gamma}_9$	$0.05 \pm 0.16 \pm 0.02$	$\bar{\Gamma}_{29}$	$0.06 \pm 0.15 \pm 0.04$
$\bar{\Gamma}_{10}$	$0.24 \pm 0.17 \pm 0.02$	$\bar{\Gamma}_{30}$	$-0.21 \pm 0.15 \pm 0.04$
$\bar{\Gamma}_{11}$	$0.06 \pm 0.13 \pm 0.01$	$\bar{\Gamma}_{31}$	$-0.07 \pm 0.16 \pm 0.01$
$\bar{\Gamma}_{12}$	$-0.01 \pm 0.13 \pm 0.02$	$\bar{\Gamma}_{32}$	$-0.16 \pm 0.17 \pm 0.02$
$\bar{\Gamma}_{13}$	$-0.08 \pm 0.12 \pm 0.01$	$\bar{\Gamma}_{33}$	$-0.04 \pm 0.17 \pm 0.02$
$\bar{\Gamma}_{14}$	$0.09 \pm 0.13 \pm 0.01$	$\bar{\Gamma}_{34}$	$0.15 \pm 0.11 \pm 0.01$
$\bar{\Gamma}_{15}$	$0.11 \pm 0.13 \pm 0.00$	$\bar{\Gamma}_{35}$	$-0.13 \pm 0.11 \pm 0.01$
$\bar{\Gamma}_{16}$	$-0.12 \pm 0.13 \pm 0.01$	$\bar{\Gamma}_{36}$	$0.05 \pm 0.11 \pm 0.01$
$\bar{\Gamma}_{17}$	$-0.04 \pm 0.13 \pm 0.01$	$\bar{\Gamma}_{37}$	$0.05 \pm 0.11 \pm 0.01$
$\bar{\Gamma}_{18}$	$0.03 \pm 0.14 \pm 0.01$	$\bar{\Gamma}_{38}$	$0.06 \pm 0.11 \pm 0.00$
$\bar{\Gamma}_{19}$	$0.11 \pm 0.11 \pm 0.01$	$\bar{\Gamma}_{39}$	$-0.08 \pm 0.11 \pm 0.00$
$\bar{\Gamma}_{20}$	$-0.00 \pm 0.11 \pm 0.01$	$\bar{\Gamma}_{40}$	$0.15 \pm 0.11 \pm 0.01$
$\bar{\Gamma}_{21}$	$0.03 \pm 0.12 \pm 0.01$	$\bar{\Gamma}_{41}$	$0.12 \pm 0.11 \pm 0.01$

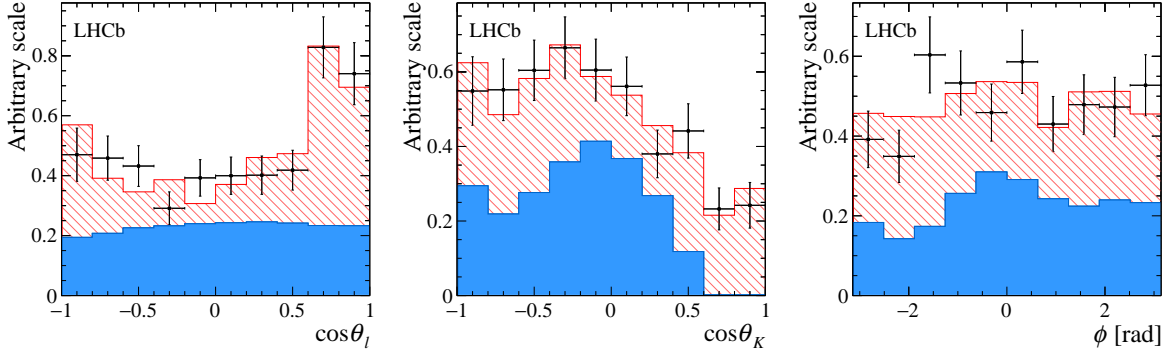


Figure 7: The distributions of each of the decay angles within the signal region. The acceptance-corrected data is represented by the points with error bars. The estimated signal distribution is shown by the blue, shaded histogram. The projected background from the upper mass sideband is shown by the red, hatched histogram, which is stacked onto the signal histogram.

acceptance function.

The effect of differences between the data candidates and the simulated candidates is evaluated using pseudoexperiments, where candidates are generated with an acceptance determined from simulated candidates without applying the corrections for the differences

Table 4: Summary of the main sources of systematic uncertainty for the differential branching fraction and the angular moments analysis. Typical ranges are quoted for the different q^2 bins used in the differential branching fraction measurement, and for the moments measured in the angular analysis. The systematic uncertainties are significantly smaller than the statistical ones.

Source	$d\mathcal{B}/dq^2 \times 10^{-8} [c^4/\text{GeV}^2]$	$\bar{\Gamma}_i$
Acceptance stat. uncertainty	0.006–0.030	0.003–0.013
Data-simulation differences	0.001–0.014	0.001–0.007
Peaking backgrounds	0.013–0.026	0.001–0.040
$\mathcal{B}(B^0 \rightarrow J/\psi K^*(892)^0)$	0.033–0.110	–

between data and simulation described in Sec. 3.

The effect of residual peaking background contributions is evaluated using pseudoexperiments, where peaking background components are generated in addition to the signal and the combinatorial background. The angular distributions of the peaking backgrounds are taken from data by isolating the decays using dedicated selections.

All other sources of systematic uncertainties investigated, such as the choice of the $m(K^+\pi^-\mu^+\mu^-)$ signal model and the resolution in the angular variables, are found to have a negligible impact.

10 Conclusions

This paper presents measurements of the differential branching fraction and angular moments of the decay $B^0 \rightarrow K^+\pi^-\mu^+\mu^-$ in the $K^+\pi^-$ invariant mass range $1330 < m(K^+\pi^-) < 1530$ MeV/ c^2 . The data sample corresponds to an integrated luminosity of 3 fb^{-1} of pp collision data collected by the LHCb experiment. The differential branching fraction is reported in five narrow q^2 bins between 0.1 and 8.0 GeV $^2/c^4$ and in the range $1.1 < q^2 < 6.0$ GeV $^2/c^4$, where an angular moments analysis is also performed.

The measured values of the angular observables $\bar{\Gamma}_2$ and $\bar{\Gamma}_3$ point towards the presence of large interference effects between the S- and P- or D-wave contributions. Using only $\bar{\Gamma}_5$ and $\bar{\Gamma}_{10}$ it is possible to estimate the D-wave fraction, F_D , yielding an upper limit of $F_D < 0.29$ at 95% confidence level. This value is lower than naively expected from amplitude analyses of $B^0 \rightarrow J/\psi K^+\pi^-$ decays [26].

The underlying Wilson coefficients may be extracted from the normalised moments and covariance matrix presented in this analysis, when combined with a prediction for the form factors. While first estimates for the form factors are given in Ref. [11], no interpretation of the results in terms of the Wilson coefficients is made at this time. With additional input from theory, these results could provide further contributions to understanding the pattern of deviations with respect to SM predictions that has been observed in other $b \rightarrow s\mu\mu$ transitions.

Acknowledgements

We express our gratitude to our colleagues in the CERN accelerator departments for the excellent performance of the LHC. We thank the technical and administrative staff at the LHCb institutes. We acknowledge support from CERN and from the national agencies: CAPES, CNPq, FAPERJ and FINEP (Brazil); NSFC (China); CNRS/IN2P3 (France); BMBF, DFG and MPG (Germany); INFN (Italy); FOM and NWO (The Netherlands); MNiSW and NCN (Poland); MEN/IFA (Romania); MinES and FASO (Russia); MinECo (Spain); SNSF and SER (Switzerland); NASU (Ukraine); STFC (United Kingdom); NSF (USA). We acknowledge the computing resources that are provided by CERN, IN2P3 (France), KIT and DESY (Germany), INFN (Italy), SURF (The Netherlands), PIC (Spain), GridPP (United Kingdom), RRCKI and Yandex LLC (Russia), CSCS (Switzerland), IFIN-HH (Romania), CBPF (Brazil), PL-GRID (Poland) and OSC (USA). We are indebted to the communities behind the multiple open source software packages on which we depend. Individual groups or members have received support from AvH Foundation (Germany), EPLANET, Marie Skłodowska-Curie Actions and ERC (European Union), Conseil Général de Haute-Savoie, Labex ENIGMASS and OCEVU, Région Auvergne (France), RFBR and Yandex LLC (Russia), GVA, XuntaGal and GENCAT (Spain), Herchel Smith Fund, The Royal Society, Royal Commission for the Exhibition of 1851 and the Leverhulme Trust (United Kingdom).

Appendices

A Angular distribution

The transversity-basis moments of the 41 orthonormal angular functions defined in Eq. 1 are shown in Table 5. The orthonormal angular basis is constructed out of spherical harmonics, $Y_l^m \equiv Y_l^m(\theta_\ell, \phi)$, and reduced spherical harmonics, $P_l^m \equiv \sqrt{2\pi}Y_l^m(\theta_K, 0)$. The S-, P- and D-wave transversity amplitudes are denoted as $S^{\{L,R\}}$, $H_{\{0,\parallel,\perp\}}^{\{L,R\}}$ and $D_{\{0,\parallel,\perp\}}^{\{L,R\}}$, respectively.

It should be noted that in addition to dependence on the amplitudes there is an overall kinematic factor of $\mathbf{k}q^2$, where \mathbf{k} is the B^0 break-up momentum given by

$$\mathbf{k} = \sqrt{\frac{(m_B^2 - q^2 + m^2(K^+\pi^-))^2}{4m_B^2} - m^2(K^+\pi^-)}, \quad (9)$$

and m_B is the B^0 mass.

Table 5: The transversity-basis moments of the 41 orthonormal angular functions $f_i(\Omega)$ in Eq. 1 [12]. The amplitudes correspond to the \bar{B}^0 decay.

i	$f_i(\Omega)$	$\Gamma_i^{L,\text{tr}}(q^2)/\mathbf{k}q^2$	$\eta_i^{L \rightarrow R}$
1	$P_0^0 Y_0^0$	$ H_0^L ^2 + H_{\parallel}^L ^2 + H_{\perp}^L ^2 + S^L ^2 + D_0^L ^2 + D_{\parallel}^L ^2 + D_{\perp}^L ^2$	+1
2	$P_1^0 Y_0^0$	$2 \left[\frac{2}{\sqrt{5}} \text{Re}(H_0^L D_0^{L*}) + \text{Re}(S^L H_0^{L*}) + \sqrt{\frac{3}{5}} \text{Re}(H_{\parallel}^L D_{\parallel}^{L*} + H_{\perp}^L D_{\perp}^{L*}) \right]$	+1
3	$P_2^0 Y_0^0$	$\frac{\sqrt{5}}{7} (D_{\parallel}^L ^2 + D_{\perp}^L ^2) - \frac{1}{\sqrt{5}} (H_{\parallel}^L ^2 + H_{\perp}^L ^2) + \frac{2}{\sqrt{5}} H_0^L ^2 + \frac{10}{7\sqrt{5}} D_0^L ^2 + 2 \text{Re}(S^L D_0^{L*})$	+1
4	$P_3^0 Y_0^0$	$\frac{6}{\sqrt{35}} \left[-\text{Re}(H_{\parallel}^L D_{\parallel}^{L*} + H_{\perp}^L D_{\perp}^{L*}) + \sqrt{3} \text{Re}(H_0^L D_0^{L*}) \right]$	+1
5	$P_4^0 Y_0^0$	$\frac{2}{7} \left[-2(D_{\parallel}^L ^2 + D_{\perp}^L ^2) + 3 D_0^L ^2 \right]$	+1
6	$P_0^0 Y_2^0$	$\frac{1}{2\sqrt{5}} \left[(D_{\parallel}^L ^2 + D_{\perp}^L ^2) + (H_{\parallel}^L ^2 + H_{\perp}^L ^2) - 2 S^L ^2 - 2 D_0^L ^2 - 2 H_0^L ^2 \right]$	+1
7	$P_1^0 Y_2^0$	$\frac{\sqrt{3}}{5} \text{Re}(H_{\parallel}^L D_{\parallel}^{L*} + H_{\perp}^L D_{\perp}^{L*}) - \frac{2}{5} \text{Re}(S^L H_0^{L*}) - \frac{4}{5} \text{Re}(H_0^L D_0^{L*})$	+1
8	$P_2^0 Y_2^0$	$\left[\frac{1}{14} (D_{\parallel}^L ^2 + D_{\perp}^L ^2) - \frac{2}{7} D_0^L ^2 - \frac{1}{10} (H_{\parallel}^L ^2 + H_{\perp}^L ^2) - \frac{2}{5} H_0^L ^2 - \frac{2}{\sqrt{5}} \text{Re}(S^L D_0^{L*}) \right]$	+1
9	$P_3^0 Y_2^0$	$-\frac{3}{5\sqrt{7}} \left[\text{Re}(H_{\parallel}^L D_{\parallel}^{L*} + H_{\perp}^L D_{\perp}^{L*}) + 2\sqrt{3} \text{Re}(H_0^L D_0^{L*}) \right]$	+1
10	$P_4^0 Y_2^0$	$-\frac{2}{7\sqrt{5}} \left[D_{\parallel}^L ^2 + D_{\perp}^L ^2 + 3 D_0^L ^2 \right]$	+1
11	$P_1^1 \sqrt{2} \text{Re}(Y_2^1)$	$-\frac{3}{\sqrt{10}} \left[\sqrt{\frac{2}{3}} \text{Re}(H_{\parallel}^L S^{L*}) - \sqrt{\frac{2}{15}} \text{Re}(H_{\parallel}^L D_0^{L*}) + \sqrt{\frac{2}{5}} \text{Re}(D_{\parallel}^L H_0^{L*}) \right]$	+1
12	$P_2^1 \sqrt{2} \text{Re}(Y_2^1)$	$-\frac{3}{5} \left[\text{Re}(H_{\parallel}^L H_0^{L*}) + \sqrt{\frac{5}{3}} \text{Re}(D_{\parallel}^L S^{L*}) + \frac{5}{7\sqrt{3}} \text{Re}(D_{\parallel}^L D_0^{L*}) \right]$	+1
13	$P_3^1 \sqrt{2} \text{Re}(Y_2^1)$	$-\frac{6}{5\sqrt{14}} \left[2 \text{Re}(D_{\parallel}^L H_0^{L*}) + \sqrt{3} \text{Re}(H_{\parallel}^L D_0^{L*}) \right]$	+1
14	$P_4^1 \sqrt{2} \text{Re}(Y_2^1)$	$-\frac{6}{7\sqrt{2}} \text{Re}(D_{\parallel}^L D_0^{L*})$	+1
15	$P_1^1 \sqrt{2} \text{Im}(Y_2^1)$	$3 \left[\frac{1}{\sqrt{15}} \text{Im}(H_{\perp}^L S^{L*}) + \frac{1}{5} \text{Im}(D_{\perp}^L H_0^{L*}) - \frac{1}{5\sqrt{3}} \text{Im}(H_{\perp}^L D_0^{L*}) \right]$	+1
16	$P_2^1 \sqrt{2} \text{Im}(Y_2^1)$	$3 \left[\frac{1}{7\sqrt{3}} \text{Im}(D_{\perp}^L D_0^{L*}) + \frac{1}{5} \text{Im}(H_{\perp}^L H_0^{L*}) + \frac{1}{\sqrt{15}} \text{Im}(D_{\perp}^L S^{L*}) \right]$	+1
17	$P_3^1 \sqrt{2} \text{Im}(Y_2^1)$	$\frac{6}{5\sqrt{14}} \left[2 \text{Im}(D_{\perp}^L H_0^{L*}) + \sqrt{3} \text{Im}(H_{\perp}^L D_0^{L*}) \right]$	+1
18	$P_4^1 \sqrt{2} \text{Im}(Y_2^1)$	$\frac{6}{7\sqrt{2}} \text{Im}(D_{\perp}^L D_0^{L*})$	+1
19	$P_0^0 \sqrt{2} \text{Re}(Y_2^2)$	$-\frac{3}{2\sqrt{15}} \left[(H_{\parallel}^L ^2 - H_{\perp}^L ^2) + (D_{\parallel}^L ^2 - D_{\perp}^L ^2) \right]$	+1
20	$P_1^0 \sqrt{2} \text{Re}(Y_2^2)$	$-\frac{3}{5} \left[\text{Re}(H_{\parallel}^L D_{\parallel}^{L*}) - \text{Re}(D_{\perp}^L H_{\perp}^{L*}) \right]$	+1
21	$P_2^0 \sqrt{2} \text{Re}(Y_2^2)$	$\frac{\sqrt{3}}{2} \left[-\frac{1}{7} (D_{\parallel}^L ^2 - D_{\perp}^L ^2) + \frac{1}{5} (H_{\parallel}^L ^2 - H_{\perp}^L ^2) \right]$	+1
22	$P_3^0 \sqrt{2} \text{Re}(Y_2^2)$	$\frac{3}{5} \sqrt{\frac{3}{7}} \left[\text{Re}(H_{\parallel}^L D_{\parallel}^{L*}) - \text{Re}(D_{\perp}^L H_{\perp}^{L*}) \right]$	+1
23	$P_4^0 \sqrt{2} \text{Re}(Y_2^2)$	$\frac{2}{7} \sqrt{\frac{3}{5}} (D_{\parallel}^L ^2 - D_{\perp}^L ^2)$	+1
24	$P_0^0 \sqrt{2} \text{Im}(Y_2^2)$	$\sqrt{\frac{3}{5}} \left[\text{Im}(H_{\perp}^L H_{\parallel}^{L*}) + \text{Im}(D_{\perp}^L D_{\parallel}^{L*}) \right]$	+1
25	$P_1^0 \sqrt{2} \text{Im}(Y_2^2)$	$\frac{3}{5} \text{Im}(H_{\perp}^L D_{\parallel}^{L*} + D_{\perp}^L H_{\parallel}^{L*})$	+1
26	$P_2^0 \sqrt{2} \text{Im}(Y_2^2)$	$\sqrt{3} \left[\frac{1}{7} \text{Im}(D_{\perp}^L D_{\parallel}^{L*}) - \frac{1}{5} \text{Im}(H_{\perp}^L H_{\parallel}^{L*}) \right]$	+1
27	$P_3^0 \sqrt{2} \text{Im}(Y_2^2)$	$-\frac{3}{5} \sqrt{\frac{3}{7}} \text{Im}(D_{\perp}^L H_{\parallel}^{L*} + H_{\perp}^L D_{\parallel}^{L*})$	+1
28	$P_4^0 \sqrt{2} \text{Im}(Y_2^2)$	$-\frac{4}{7} \sqrt{\frac{3}{5}} \text{Im}(D_{\perp}^L D_{\parallel}^{L*})$	+1
29	$P_0^0 Y_1^0$	$-\sqrt{3} \left[\text{Re}(H_{\perp}^L H_{\parallel}^{L*}) + \text{Re}(D_{\perp}^L D_{\parallel}^{L*}) \right]$	-1
30	$P_1^0 Y_1^0$	$-\frac{3}{\sqrt{5}} \text{Re}(H_{\perp}^L D_{\parallel}^{L*} + H_{\parallel}^L D_{\perp}^{L*})$	-1
31	$P_2^0 Y_1^0$	$-\frac{3}{\sqrt{15}} \left[\frac{5}{7} \text{Re}(D_{\perp}^L D_{\parallel}^{L*}) - \text{Re}(H_{\perp}^L H_{\parallel}^{L*}) \right]$	-1
32	$P_3^0 Y_1^0$	$\frac{9}{\sqrt{105}} \text{Re}(H_{\perp}^L D_{\parallel}^{L*} + H_{\parallel}^L D_{\perp}^{L*})$	-1
33	$P_4^0 Y_1^0$	$\frac{4\sqrt{3}}{7} \text{Re}(D_{\perp}^L D_{\parallel}^{L*})$	-1
34	$P_1^1 \sqrt{2} \text{Re}(Y_1^1)$	$\sqrt{\frac{3}{5}} \left[\sqrt{5} \text{Re}(H_{\perp}^L S^{L*}) + \sqrt{3} \text{Re}(D_{\perp}^L H_0^{L*}) - \text{Re}(H_{\perp}^L D_0^{L*}) \right]$	-1
35	$P_2^1 \sqrt{2} \text{Re}(Y_1^1)$	$3 \left[\frac{1}{\sqrt{5}} \text{Re}(H_{\perp}^L H_0^{L*}) + \frac{1}{\sqrt{3}} \text{Re}(D_{\perp}^L S^{L*}) + \frac{5}{21} \sqrt{\frac{3}{5}} \text{Re}(D_{\perp}^L D_0^{L*}) \right]$	-1
36	$P_3^1 \sqrt{2} \text{Re}(Y_1^1)$	$\frac{6}{\sqrt{70}} \left[2 \text{Re}(D_{\perp}^L H_0^{L*}) + \sqrt{3} \text{Re}(H_{\perp}^L D_0^{L*}) \right]$	-1
37	$P_4^1 \sqrt{2} \text{Re}(Y_1^1)$	$\frac{3\sqrt{10}}{7} \text{Re}(D_{\perp}^L D_0^{L*})$	-1
38	$P_1^1 \sqrt{2} \text{Im}(Y_1^1)$	$-\sqrt{\frac{3}{5}} \left[\sqrt{5} \text{Im}(H_{\parallel}^L S^{L*}) + \sqrt{3} \text{Im}(D_{\parallel}^L H_0^{L*}) - \text{Im}(H_{\parallel}^L D_0^{L*}) \right]$	-1
39	$P_2^1 \sqrt{2} \text{Im}(Y_1^1)$	$-\sqrt{\frac{3}{5}} \left[\sqrt{3} \text{Im}(H_{\parallel}^L H_0^{L*}) + \sqrt{5} \text{Im}(D_{\parallel}^L S^{L*}) + \frac{5}{7} \text{Im}(D_{\parallel}^L D_0^{L*}) \right]$	-1
40	$P_3^1 \sqrt{2} \text{Im}(Y_1^1)$	$-6\sqrt{\frac{3}{70}} \left[2 \text{Im}(D_{\parallel}^L H_0^{L*}) + \sqrt{3} \text{Im}(H_{\parallel}^L D_0^{L*}) \right]$	-1
41	$P_4^1 \sqrt{2} \text{Im}(Y_1^1)$	$-\frac{3}{7} \sqrt{10} \text{Im}(D_{\parallel}^L D_0^{L*})$	-1

B Mass distributions

Figure 8 shows the fits to the $m(K^+\pi^-\mu^+\mu^-)$ distribution in each of the q^2 bins used for the differential branching fraction measurement.

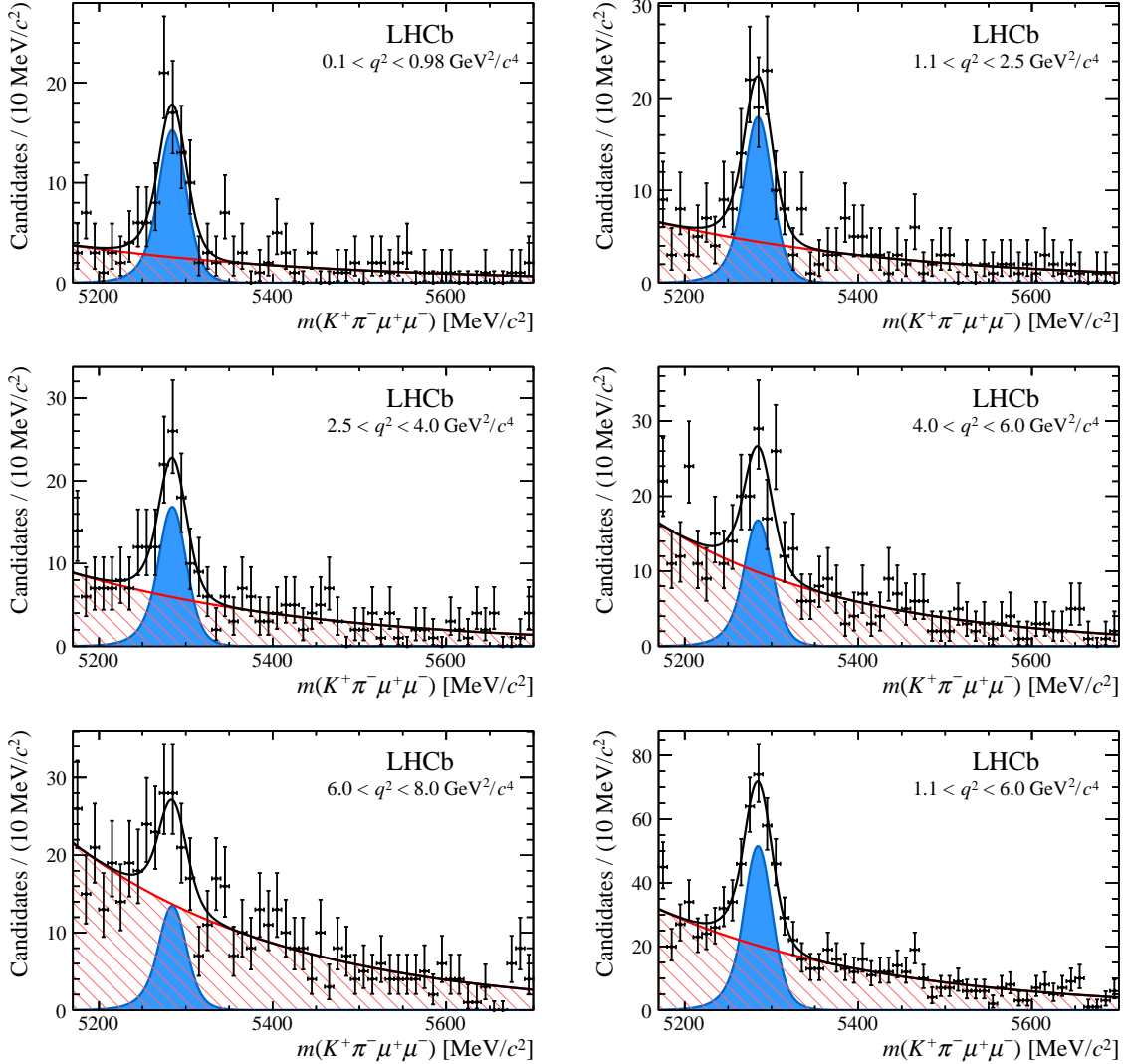


Figure 8: Invariant mass $m(K^+\pi^-\mu^+\mu^-)$ distributions of the signal decay $B^0 \rightarrow K^+\pi^-\mu^+\mu^-$ in each of the q^2 bins used for the differential branching fraction measurement. The solid black line represents the total fitted function. The individual components of the signal (blue, shaded area) and combinatorial background (red, hatched area) are also shown.

References

- [1] LHCb collaboration, R. Aaij *et al.*, *Differential branching fraction and angular analysis of the decay $B^0 \rightarrow K^{*0}\mu^+\mu^-$* , Phys. Rev. Lett. **108** (2012) 181806, [arXiv:1112.3515](#).
- [2] LHCb collaboration, R. Aaij *et al.*, *Differential branching fraction and angular analysis of the decay $B^0 \rightarrow K^{*0}\mu^+\mu^-$* , JHEP **08** (2013) 131, [arXiv:1304.6325](#).
- [3] LHCb collaboration, R. Aaij *et al.*, *Measurement of form-factor-independent observables in the decay $B^0 \rightarrow K^{*0}\mu^+\mu^-$* , Phys. Rev. Lett. **111** (2013) 191801, [arXiv:1308.1707](#).
- [4] LHCb collaboration, R. Aaij *et al.*, *Angular analysis of the $B^0 \rightarrow K^{*0}\mu^+\mu^-$ decay using 3 fb^{-1} of integrated luminosity*, JHEP **02** (2016) 104, [arXiv:1512.04442](#).
- [5] S. Descotes-Genon, J. Matias, and J. Virto, *Understanding the $B \rightarrow K^*\mu^+\mu^-$ anomaly*, Phys. Rev. **D88** (2013) 074002, [arXiv:1307.5683](#).
- [6] F. Beaujean, C. Bobeth, and D. van Dyk, *Comprehensive Bayesian analysis of rare (semi)leptonic and radiative B decays*, Eur. Phys. J. **C74** (2014) 2897, [arXiv:1310.2478](#), [Erratum: Eur. Phys. J. **C74** (2014) 3179].
- [7] A. Crivellin, G. D'Ambrosio, and J. Heeck, *Explaining $h \rightarrow \mu^\pm\tau^\mp$, $B \rightarrow K^*\mu^+\mu^-$ and $B \rightarrow K\mu^+\mu^-/B \rightarrow Ke^+e^-$ in a two-Higgs-doublet model with gauged $L_\mu - L_\tau$* , Phys. Rev. Lett. **114** (2015) 151801, [arXiv:1501.00993](#).
- [8] J. Lyon and R. Zwicky, *Resonances gone topsy turvy - the charm of QCD or new physics in $b \rightarrow s\ell^+\ell^-$?*, [arXiv:1406.0566](#).
- [9] LHCb collaboration, R. Aaij *et al.*, *Measurement of the S-wave fraction in $B^0 \rightarrow K^+\pi^-\mu^+\mu^-$ decays and the $B^0 \rightarrow K^*(892)^0\mu^+\mu^-$ differential branching fraction*, [arXiv:1606.04731](#), submitted to JHEP.
- [10] K. A. Olive, *Review of Particle Physics*, Chin. Phys. **C40** (2016), no. 10 100001.
- [11] C.-D. Lu and W. Wang, *Analysis of $B \rightarrow K_j^*(\rightarrow K\pi)\mu^+\mu^-$ in the higher kaon resonance region*, Phys. Rev. **D85** (2012) 034014, [arXiv:1111.1513](#).
- [12] B. Dey, *Angular analyses of exclusive $\bar{B} \rightarrow X\ell_1\ell_2$ with complex helicity amplitudes*, Phys. Rev. **D92** (2015) 033013, [arXiv:1505.02873](#).
- [13] M. Pivk and F. R. Le Diberder, *sPlot: A statistical tool to unfold data distributions*, Nucl. Instrum. Meth. **A555** (2005) 356, [arXiv:physics/0402083](#).
- [14] LHCb collaboration, A. A. Alves Jr. *et al.*, *The LHCb detector at the LHC*, JINST **3** (2008) S08005.
- [15] LHCb collaboration, R. Aaij *et al.*, *LHCb detector performance*, Int. J. Mod. Phys. **A30** (2015) 1530022, [arXiv:1412.6352](#).
- [16] T. Sjöstrand, S. Mrenna, and P. Skands, *PYTHIA 6.4 physics and manual*, JHEP **05** (2006) 026, [arXiv:hep-ph/0603175](#).

- [17] T. Sjöstrand, S. Mrenna, and P. Skands, *A brief introduction to PYTHIA 8.1*, Comput. Phys. Commun. **178** (2008) 852, arXiv:0710.3820.
- [18] I. Belyaev *et al.*, *Handling of the generation of primary events in Gauss, the LHCb simulation framework*, J. Phys. Conf. Ser. **331** (2011) 032047.
- [19] D. J. Lange, *The EvtGen particle decay simulation package*, Nucl. Instrum. Meth. **A462** (2001) 152.
- [20] P. Golonka and Z. Was, *PHOTOS Monte Carlo: A precision tool for QED corrections in Z and W decays*, Eur. Phys. J. **C45** (2006) 97, arXiv:hep-ph/0506026.
- [21] Geant4 collaboration, J. Allison *et al.*, *Geant4 developments and applications*, IEEE Trans. Nucl. Sci. **53** (2006) 270.
- [22] M. Clemencic *et al.*, *The LHCb simulation application, Gauss: Design, evolution and experience*, J. Phys. Conf. Ser. **331** (2011) 032023.
- [23] L. Breiman, J. H. Friedman, R. A. Olshen, and C. J. Stone, *Classification and regression trees*, Wadsworth international group, Belmont, California, USA, 1984.
- [24] R. E. Schapire and Y. Freund, *A decision-theoretic generalization of on-line learning and an application to boosting*, J. Comput. Syst. Sci. **55** (1997) 119.
- [25] LHCb collaboration, R. Aaij *et al.*, *Measurement of the polarization amplitudes in $B^0 \rightarrow J/\psi K^*(892)^0$ decays*, Phys. Rev. **D88** (2013) 052002, arXiv:1307.2782.
- [26] Belle collaboration, K. Chilikin *et al.*, *Observation of a new charged charmoniumlike state in $\bar{B}^0 \rightarrow J/\psi K^- \pi^+$ decays*, Phys. Rev. **D90** (2014) 112009, arXiv:1408.6457.
- [27] F. Beaujean, M. Chrzyszcz, N. Serra, and D. van Dyk, *Extracting Angular Observables without a Likelihood and Applications to Rare Decays*, Phys. Rev. **D91** (2015), no. 11 114012, arXiv:1503.04100.
- [28] J. Gratx, M. Hopfer, and R. Zwicky, *Generalised helicity formalism, higher moments and the $B \rightarrow K_{J_K}(\rightarrow K\pi)\bar{\ell}_1\ell_2$ angular distributions*, Phys. Rev. **D93** (2016), no. 5 054008, arXiv:1506.03970.
- [29] HepData website, <https://www.hepdata.net/record/ins1486676>.
- [30] G. J. Feldman and R. D. Cousins, *A Unified approach to the classical statistical analysis of small signals*, Phys. Rev. **D57** (1998) 3873, arXiv:physics/9711021.

LHCb collaboration

R. Aaij⁴⁰, B. Adeva³⁹, M. Adinolfi⁴⁸, Z. Ajaltouni⁵, S. Akar⁶, J. Albrecht¹⁰, F. Alessio⁴⁰, M. Alexander⁵³, S. Ali⁴³, G. Alkhazov³¹, P. Alvarez Cartelle⁵⁵, A.A. Alves Jr⁵⁹, S. Amato², S. Amerio²³, Y. Amhis⁷, L. An⁴¹, L. Anderlini¹⁸, G. Andreassi⁴¹, M. Andreotti^{17,g}, J.E. Andrews⁶⁰, R.B. Appleby⁵⁶, F. Archilli⁴³, P. d'Argent¹², J. Arnau Romeu⁶, A. Artamonov³⁷, M. Artuso⁶¹, E. Aslanides⁶, G. Auriemma²⁶, M. Baalouch⁵, I. Babuschkin⁵⁶, S. Bachmann¹², J.J. Back⁵⁰, A. Badalov³⁸, C. Baesso⁶², W. Baldini¹⁷, R.J. Barlow⁵⁶, C. Barschel⁴⁰, S. Barsuk⁷, W. Barter⁴⁰, M. Baszczyk²⁷, V. Batozskaya²⁹, B. Batsukh⁶¹, V. Battista⁴¹, A. Bay⁴¹, L. Beaucourt⁴, J. Beddow⁵³, F. Bedeschi²⁴, I. Bediaga¹, L.J. Bel⁴³, V. Bellee⁴¹, N. Belloli^{21,i}, K. Belous³⁷, I. Belyaev³², E. Ben-Haim⁸, G. Bencivenni¹⁹, S. Benson⁴³, J. Benton⁴⁸, A. Berezhnoy³³, R. Bernet⁴², A. Bertolin²³, F. Betti¹⁵, M.-O. Bettler⁴⁰, M. van Beuzekom⁴³, I. Bezshyiko⁴², S. Bifani⁴⁷, P. Billoir⁸, T. Bird⁵⁶, A. Birnkraut¹⁰, A. Bitadze⁵⁶, A. Bizzeti^{18,u}, T. Blake⁵⁰, F. Blanc⁴¹, J. Blouw¹¹, S. Blusk⁶¹, V. Bocci²⁶, T. Boettcher⁵⁸, A. Bondar³⁶, N. Bondar^{31,40}, W. Bonivento¹⁶, A. Borgheresi^{21,i}, S. Borghi⁵⁶, M. Borisyak³⁵, M. Borsato³⁹, F. Bossu⁷, M. Boubdir⁹, T.J.V. Bowcock⁵⁴, E. Bowen⁴², C. Bozzi^{17,40}, S. Braun¹², M. Britsch¹², T. Britton⁶¹, J. Brodzicka⁵⁶, E. Buchanan⁴⁸, C. Burr⁵⁶, A. Bursche², J. Buytaert⁴⁰, S. Cadeddu¹⁶, R. Calabrese^{17,g}, M. Calvi^{21,i}, M. Calvo Gomez^{38,m}, A. Camboni³⁸, P. Campana¹⁹, D. Campora Perez⁴⁰, D.H. Campora Perez⁴⁰, L. Capriotti⁵⁶, A. Carbone^{15,e}, G. Carboni^{25,j}, R. Cardinale^{20,h}, A. Cardini¹⁶, P. Carniti^{21,i}, L. Carson⁵², K. Carvalho Akiba², G. Casse⁵⁴, L. Cassina^{21,i}, L. Castillo Garcia⁴¹, M. Cattaneo⁴⁰, Ch. Cauet¹⁰, G. Cavallero²⁰, R. Cenci^{24,t}, M. Charles⁸, Ph. Charpentier⁴⁰, G. Chatzikonstantinidis⁴⁷, M. Chefdeville⁴, S. Chen⁵⁶, S.-F. Cheung⁵⁷, V. Chobanova³⁹, M. Chrzaszcz^{42,27}, X. Cid Vidal³⁹, G. Ciezarek⁴³, P.E.L. Clarke⁵², M. Clemencic⁴⁰, H.V. Cliff⁴⁹, J. Closier⁴⁰, V. Coco⁵⁹, J. Cogan⁶, E. Cogneras⁵, V. Cogoni^{16,40,f}, L. Cojocariu³⁰, G. Collazuol^{23,o}, P. Collins⁴⁰, A. Comerma-Montells¹², A. Contu⁴⁰, A. Cook⁴⁸, S. Coquereau⁸, G. Corti⁴⁰, M. Corvo^{17,g}, C.M. Costa Sobral⁵⁰, B. Couturier⁴⁰, G.A. Cowan⁵², D.C. Craik⁵², A. Crocombe⁵⁰, M. Cruz Torres⁶², S. Cunliffe⁵⁵, R. Currie⁵⁵, C. D'Ambrosio⁴⁰, E. Dall'Occo⁴³, J. Dalseno⁴⁸, P.N.Y. David⁴³, A. Davis⁵⁹, O. De Aguiar Francisco², K. De Bruyn⁶, S. De Capua⁵⁶, M. De Cian¹², J.M. De Miranda¹, L. De Paula², M. De Serio^{14,d}, P. De Simone¹⁹, C.-T. Dean⁵³, D. Decamp⁴, M. Deckenhoff¹⁰, L. Del Buono⁸, M. Demmer¹⁰, D. Derkach³⁵, O. Deschamps⁵, F. Dettori⁴⁰, B. Dey²², A. Di Canto⁴⁰, H. Dijkstra⁴⁰, F. Dordei⁴⁰, M. Dorigo⁴¹, A. Dosil Suárez³⁹, A. Dovbnya⁴⁵, K. Dreimanis⁵⁴, L. Dufour⁴³, G. Dujany⁵⁶, K. Dungs⁴⁰, P. Durante⁴⁰, R. Dzhelyadin³⁷, A. Dziurda⁴⁰, A. Dzyuba³¹, N. Déleage⁴, S. Easo⁵¹, M. Ebert⁵², U. Egede⁵⁵, V. Egorychev³², S. Eidelman³⁶, S. Eisenhardt⁵², U. Eitschberger¹⁰, R. Ekelhof¹⁰, L. Eklund⁵³, Ch. Elsasser⁴², S. Ely⁶¹, S. Esen¹², H.M. Evans⁴⁹, T. Evans⁵⁷, A. Falabella¹⁵, N. Farley⁴⁷, S. Farry⁵⁴, R. Fay⁵⁴, D. Fazzini^{21,i}, D. Ferguson⁵², V. Fernandez Albor³⁹, A. Fernandez Prieto³⁹, F. Ferrari^{15,40}, F. Ferreira Rodrigues¹, M. Ferro-Luzzi⁴⁰, S. Filippov³⁴, R.A. Fini¹⁴, M. Fiore^{17,g}, M. Fiorini^{17,g}, M. Firlej²⁸, C. Fitzpatrick⁴¹, T. Fiutowski²⁸, F. Fleuret^{7,b}, K. Fohl⁴⁰, M. Fontana¹⁶, F. Fontanelli^{20,h}, D.C. Forshaw⁶¹, R. Forty⁴⁰, V. Franco Lima⁵⁴, M. Frank⁴⁰, C. Frei⁴⁰, J. Fu^{22,q}, E. Furfaro^{25,j}, C. Färber⁴⁰, A. Gallas Torreira³⁹, D. Galli^{15,e}, S. Gallorini²³, S. Gambetta⁵², M. Gandelman², P. Gandini⁵⁷, Y. Gao³, L.M. Garcia Martin⁶⁸, J. García Pardiñas³⁹, J. Garra Tico⁴⁹, L. Garrido³⁸, P.J. Garsed⁴⁹, D. Gascon³⁸, C. Gaspar⁴⁰, L. Gavardi¹⁰, G. Gazzoni⁵, D. Gerick¹², E. Gersabeck¹², M. Gersabeck⁵⁶, T. Gershon⁵⁰, Ph. Ghez⁴, S. Giani⁴¹, V. Gibson⁴⁹, O.G. Girard⁴¹, L. Giubega³⁰, K. Gizdov⁵², V.V. Gligorov⁸, D. Golubkov³², A. Golutvin^{55,40}, A. Gomes^{1,a}, I.V. Gorelov³³, C. Gotti^{21,i}, M. Grabalosa Gándara⁵, R. Graciani Diaz³⁸, L.A. Granado Cardoso⁴⁰, E. Graugés³⁸, E. Graverini⁴², G. Graziani¹⁸, A. Greco³⁰, P. Griffith⁴⁷, L. Grillo^{21,i}, B.R. Gruber Cazon⁵⁷, O. Grünberg⁶⁶, E. Gushchin³⁴, Yu. Guz³⁷, T. Gys⁴⁰, C. Göbel⁶², T. Hadavizadeh⁵⁷, C. Hadjivasiliou⁵, G. Haefeli⁴¹, C. Haen⁴⁰, S.C. Haines⁴⁹,

S. Hall⁵⁵, B. Hamilton⁶⁰, X. Han¹², S. Hansmann-Menzemer¹², N. Harnew⁵⁷, S.T. Harnew⁴⁸,
 J. Harrison⁵⁶, M. Hatch⁴⁰, J. He⁶³, T. Head⁴¹, A. Heister⁹, K. Hennessy⁵⁴, P. Henrard⁵,
 L. Henry⁸, J.A. Hernando Morata³⁹, E. van Herwijnen⁴⁰, M. Heß⁶⁶, A. Hicheur², D. Hill⁵⁷,
 C. Hombach⁵⁶, H. Hopchev⁴¹, W. Hulsbergen⁴³, T. Humair⁵⁵, M. Hushchyn³⁵, N. Hussain⁵⁷,
 D. Hutchcroft⁵⁴, M. Idzik²⁸, P. Ilten⁵⁸, R. Jacobsson⁴⁰, A. Jaeger¹², J. Jalocha⁵⁷, E. Jans⁴³,
 A. Jawahery⁶⁰, M. John⁵⁷, D. Johnson⁴⁰, C.R. Jones⁴⁹, C. Joram⁴⁰, B. Jost⁴⁰, N. Jurik⁶¹,
 S. Kandybei⁴⁵, W. Kanso⁶, M. Karacson⁴⁰, J.M. Kariuki⁴⁸, S. Karodia⁵³, M. Kecke¹²,
 M. Kelsey⁶¹, I.R. Kenyon⁴⁷, M. Kenzie⁴⁰, T. Ketel⁴⁴, E. Khairullin³⁵, B. Khanji^{21,40,i},
 C. Khurewathanakul⁴¹, T. Kirn⁹, S. Klaver⁵⁶, K. Klimaszewski²⁹, S. Koliiev⁴⁶, M. Kolpin¹²,
 I. Komarov⁴¹, R.F. Koopman⁴⁴, P. Koppenburg⁴³, A. Kozachuk³³, M. Kozeiha⁵, L. Kravchuk³⁴,
 K. Kreplin¹², M. Kreps⁵⁰, P. Krokovny³⁶, F. Kruse¹⁰, W. Krzemien²⁹, W. Kucewicz^{27,l},
 M. Kucharczyk²⁷, V. Kudryavtsev³⁶, A.K. Kuonen⁴¹, K. Kurek²⁹, T. Kvaratskheliya^{32,40},
 D. Lacarrere⁴⁰, G. Lafferty^{56,40}, A. Lai¹⁶, D. Lambert⁵², G. Lanfranchi¹⁹, C. Langenbruch⁹,
 B. Langhans⁴⁰, T. Latham⁵⁰, C. Lazzeroni⁴⁷, R. Le Gac⁶, J. van Leerdam⁴³, J.-P. Lees⁴,
 A. Leflat^{33,40}, J. Lefrançois⁷, R. Lefèvre⁵, F. Lemaitre⁴⁰, E. Lemos Cid³⁹, O. Leroy⁶, T. Lesiak²⁷,
 B. Leverington¹², Y. Li⁷, T. Likhomanenko^{35,67}, R. Lindner⁴⁰, C. Linn⁴⁰, F. Lionetto⁴²,
 B. Liu¹⁶, X. Liu³, D. Loh⁵⁰, I. Longstaff⁵³, J.H. Lopes², D. Lucchesi^{23,o}, M. Lucio Martinez³⁹,
 H. Luo⁵², A. Lupato²³, E. Luppi^{17,g}, O. Lupton⁵⁷, A. Lusiani²⁴, X. Lyu⁶³, F. Machefert⁷,
 F. Maciuc³⁰, O. Maev³¹, K. Maguire⁵⁶, S. Malde⁵⁷, A. Malinin⁶⁷, T. Maltsev³⁶, G. Manca⁷,
 G. Mancinelli⁶, P. Manning⁶¹, J. Maratas^{5,v}, J.F. Marchand⁴, U. Marconi¹⁵, C. Marin Benito³⁸,
 P. Marino^{24,t}, J. Marks¹², G. Martellotti²⁶, M. Martin⁶, M. Martinelli⁴¹, D. Martinez Santos³⁹,
 F. Martinez Vidal⁶⁸, D. Martins Tostes², L.M. Massacrier⁷, A. Massafferri¹, R. Matev⁴⁰,
 A. Mathad⁵⁰, Z. Mathe⁴⁰, C. Matteuzzi²¹, A. Mauri⁴², B. Maurin⁴¹, A. Mazurov⁴⁷,
 M. McCann⁵⁵, J. McCarthy⁴⁷, A. McNab⁵⁶, R. McNulty¹³, B. Meadows⁵⁹, F. Meier¹⁰,
 M. Meissner¹², D. Melnychuk²⁹, M. Merk⁴³, A. Merli^{22,q}, E. Michielin²³, D.A. Milanes⁶⁵,
 M.-N. Minard⁴, D.S. Mitzel¹², A. Mogini⁸, J. Molina Rodriguez⁶², I.A. Monroy⁶⁵, S. Monteil⁵,
 M. Morandin²³, P. Morawski²⁸, A. Mordà⁶, M.J. Morello^{24,t}, J. Moron²⁸, A.B. Morris⁵²,
 R. Mountain⁶¹, F. Muheim⁵², M. Mulder⁴³, M. Mussini¹⁵, D. Müller⁵⁶, J. Müller¹⁰, K. Müller⁴²,
 V. Müller¹⁰, P. Naik⁴⁸, T. Nakada⁴¹, R. Nandakumar⁵¹, A. Nandi⁵⁷, I. Nasteva²,
 M. Needham⁵², N. Neri²², S. Neubert¹², N. Neufeld⁴⁰, M. Neuner¹², A.D. Nguyen⁴¹,
 C. Nguyen-Mau^{41,n}, S. Nieswand⁹, R. Niet¹⁰, N. Nikitin³³, T. Nikodem¹², A. Novoselov³⁷,
 D.P. O'Hanlon⁵⁰, A. Oblakowska-Mucha²⁸, V. Obraztsov³⁷, S. Ogilvy¹⁹, R. Oldeman⁴⁹,
 C.J.G. Onderwater⁶⁹, J.M. Otalora Goicochea², A. Otto⁴⁰, P. Owen⁴², A. Oyanguren⁶⁸,
 P.R. Pais⁴¹, A. Palano^{14,d}, F. Palombo^{22,q}, M. Palutan¹⁹, J. Panman⁴⁰, A. Papanestis⁵¹,
 M. Pappagallo^{14,d}, L.L. Pappalardo^{17,g}, W. Parker⁶⁰, C. Parkes⁵⁶, G. Passaleva¹⁸,
 A. Pastore^{14,d}, G.D. Patel⁵⁴, M. Patel⁵⁵, C. Patrignani^{15,e}, A. Pearce^{56,51}, A. Pellegrino⁴³,
 G. Penso^{26,k}, M. Pepe Altarelli⁴⁰, S. Perazzini⁴⁰, P. Perret⁵, L. Pescatore⁴⁷, K. Petridis⁴⁸,
 A. Petrolini^{20,h}, A. Petrov⁶⁷, M. Petruzzo^{22,q}, E. Picatoste Olloqui³⁸, B. Pietrzyk⁴, M. Pikies²⁷,
 D. Pinci²⁶, A. Pistone²⁰, A. Piucci¹², S. Playfer⁵², M. Plo Casasus³⁹, T. Poikela⁴⁰, F. Polci⁸,
 A. Poluektov^{50,36}, I. Polyakov⁶¹, E. Polcarpo², G.J. Pomery⁴⁸, A. Popov³⁷, D. Popov^{11,40},
 B. Popovici³⁰, S. Poslavskii³⁷, C. Potterat², E. Price⁴⁸, J.D. Price⁵⁴, J. Prisciandaro³⁹,
 A. Pritchard⁵⁴, C. Prouve⁴⁸, V. Pugatch⁴⁶, A. Puig Navarro⁴¹, G. Punzi^{24,p}, W. Qian⁵⁷,
 R. Quagliani^{7,48}, B. Rachwal²⁷, J.H. Rademacker⁴⁸, M. Rama²⁴, M. Ramos Pernas³⁹,
 M.S. Rangel², I. Raniuk⁴⁵, G. Raven⁴⁴, F. Redi⁵⁵, S. Reichert¹⁰, A.C. dos Reis¹,
 C. Remon Alepuz⁶⁸, V. Renaudin⁷, S. Ricciardi⁵¹, S. Richards⁴⁸, M. Rühl⁴⁰, K. Rinnert^{54,40},
 V. Rives Molina³⁸, P. Robbe^{7,40}, A.B. Rodrigues¹, E. Rodrigues⁵⁹, J.A. Rodriguez Lopez⁶⁵,
 P. Rodriguez Perez⁵⁶, A. Rogozhnikov³⁵, S. Roiser⁴⁰, V. Romanovskiy³⁷, A. Romero Vidal³⁹,
 J.W. Ronayne¹³, M. Rotondo¹⁹, M.S. Rudolph⁶¹, T. Ruf⁴⁰, P. Ruiz Valls⁶⁸,
 J.J. Saborido Silva³⁹, E. Sadykhov³², N. Sagidova³¹, B. Saitta^{16,f}, V. Salustino Guimaraes²,
 C. Sanchez Mayordomo⁶⁸, B. Sanmartin Sedes³⁹, R. Santacesaria²⁶, C. Santamarina Rios³⁹,

M. Santimaria¹⁹, E. Santovetti^{25,j}, A. Sarti^{19,k}, C. Satriano^{26,s}, A. Satta²⁵, D.M. Saunders⁴⁸, D. Savrina^{32,33}, S. Schael⁹, M. Schellenberg¹⁰, M. Schiller⁴⁰, H. Schindler⁴⁰, M. Schlupp¹⁰, M. Schmelling¹¹, T. Schmelzer¹⁰, B. Schmidt⁴⁰, O. Schneider⁴¹, A. Schopper⁴⁰, K. Schubert¹⁰, M. Schubiger⁴¹, M.-H. Schune⁷, R. Schwemmer⁴⁰, B. Sciascia¹⁹, A. Sciubba^{26,k}, A. Semennikov³², A. Sergi⁴⁷, N. Serra⁴², J. Serrano⁶, L. Sestini²³, P. Seyfert²¹, M. Shapkin³⁷, I. Shapoval^{17,45,g}, Y. Shcheglov³¹, T. Shears⁵⁴, L. Shekhtman³⁶, V. Shevchenko⁶⁷, A. Shires¹⁰, B.G. Siddi¹⁷, R. Silva Coutinho⁴², L. Silva de Oliveira², G. Simi^{23,o}, S. Simone^{14,d}, M. Sirendi⁴⁹, N. Skidmore⁴⁸, T. Skwarnicki⁶¹, E. Smith⁵⁵, I.T. Smith⁵², J. Smith⁴⁹, M. Smith⁵⁵, H. Snoek⁴³, M.D. Sokoloff⁵⁹, F.J.P. Soler⁵³, D. Souza⁴⁸, B. Souza De Paula², B. Spaan¹⁰, P. Spradlin⁵³, S. Sridharan⁴⁰, F. Stagni⁴⁰, M. Stahl¹², S. Stahl⁴⁰, P. Stefko⁴¹, S. Stefkova⁵⁵, O. Steinkamp⁴², S. Stemmler¹², O. Stenyakin³⁷, S. Stevenson⁵⁷, S. Stoica³⁰, S. Stone⁶¹, B. Storaci⁴², S. Stracka^{24,p}, M. Straticiu³⁰, U. Straumann⁴², L. Sun⁵⁹, W. Sutcliffe⁵⁵, K. Swientek²⁸, V. Syropoulos⁴⁴, M. Szczekowski²⁹, T. Szumlak²⁸, S. T’Jampens⁴, A. Tayduganov⁶, T. Tekampe¹⁰, G. Tellarini^{17,g}, F. Teubert⁴⁰, C. Thomas⁵⁷, E. Thomas⁴⁰, J. van Tilburg⁴³, V. Tisserand⁴, M. Tobin⁴¹, S. Tolk⁴⁹, L. Tomassetti^{17,g}, D. Tonelli⁴⁰, S. Topp-Joergensen⁵⁷, F. Toriello⁶¹, E. Tournefier⁴, S. Tourneur⁴¹, K. Trabelsi⁴¹, M. Traill⁵³, M.T. Tran⁴¹, M. Tresch⁴², A. Trisovic⁴⁰, A. Tsaregorodtsev⁶, P. Tsopelas⁴³, A. Tully⁴⁹, N. Tuning⁴³, A. Ukleja²⁹, A. Ustyuzhanin^{35,67}, U. Uwer¹², C. Vacca^{16,40,f}, V. Vagnoni^{15,40}, A. Valassi⁴⁰, S. Valat⁴⁰, G. Valenti¹⁵, A. Vallier⁷, R. Vazquez Gomez¹⁹, P. Vazquez Regueiro³⁹, S. Vecchi¹⁷, M. van Veghel⁴³, J.J. Velthuis⁴⁸, M. Veltri^{18,r}, G. Veneziano⁴¹, A. Venkateswaran⁶¹, M. Vernet⁵, M. Vesterinen¹², B. Viaud⁷, D. Vieira¹, M. Vieites Diaz³⁹, X. Vilasis-Cardona^{38,m}, V. Volkov³³, A. Vollhardt⁴², B. Voneki⁴⁰, A. Vorobyev³¹, V. Vorobyev³⁶, C. Voß⁶⁶, J.A. de Vries⁴³, C. Vázquez Sierra³⁹, R. Waldi⁶⁶, C. Wallace⁵⁰, R. Wallace¹³, J. Walsh²⁴, J. Wang⁶¹, D.R. Ward⁴⁹, H.M. Wark⁵⁴, N.K. Watson⁴⁷, D. Websdale⁵⁵, A. Weiden⁴², M. Whitehead⁴⁰, J. Wicht⁵⁰, G. Wilkinson^{57,40}, M. Wilkinson⁶¹, M. Williams⁴⁰, M.P. Williams⁴⁷, M. Williams⁵⁸, T. Williams⁴⁷, F.F. Wilson⁵¹, J. Wimberley⁶⁰, J. Wishahi¹⁰, W. Wislicki²⁹, M. Witek²⁷, G. Wormser⁷, S.A. Wotton⁴⁹, K. Wraight⁵³, S. Wright⁴⁹, K. Wyllie⁴⁰, Y. Xie⁶⁴, Z. Xing⁶¹, Z. Xu⁴¹, Z. Yang³, H. Yin⁶⁴, J. Yu⁶⁴, X. Yuan³⁶, O. Yushchenko³⁷, M. Zangoli¹⁵, K.A. Zarebski⁴⁷, M. Zavertyaev^{11,c}, L. Zhang³, Y. Zhang⁷, Y. Zhang⁶³, A. Zhelezov¹², Y. Zheng⁶³, A. Zhokhov³², X. Zhu³, V. Zhukov⁹, S. Zucchelli¹⁵.

¹ Centro Brasileiro de Pesquisas Físicas (CBPF), Rio de Janeiro, Brazil

² Universidade Federal do Rio de Janeiro (UFRJ), Rio de Janeiro, Brazil

³ Center for High Energy Physics, Tsinghua University, Beijing, China

⁴ LAPP, Université Savoie Mont-Blanc, CNRS/IN2P3, Annecy-Le-Vieux, France

⁵ Clermont Université, Université Blaise Pascal, CNRS/IN2P3, LPC, Clermont-Ferrand, France

⁶ CPPM, Aix-Marseille Université, CNRS/IN2P3, Marseille, France

⁷ LAL, Université Paris-Sud, CNRS/IN2P3, Orsay, France

⁸ LPNHE, Université Pierre et Marie Curie, Université Paris Diderot, CNRS/IN2P3, Paris, France

⁹ I. Physikalisches Institut, RWTH Aachen University, Aachen, Germany

¹⁰ Fakultät Physik, Technische Universität Dortmund, Dortmund, Germany

¹¹ Max-Planck-Institut für Kernphysik (MPIK), Heidelberg, Germany

¹² Physikalisches Institut, Ruprecht-Karls-Universität Heidelberg, Heidelberg, Germany

¹³ School of Physics, University College Dublin, Dublin, Ireland

¹⁴ Sezione INFN di Bari, Bari, Italy

¹⁵ Sezione INFN di Bologna, Bologna, Italy

¹⁶ Sezione INFN di Cagliari, Cagliari, Italy

¹⁷ Sezione INFN di Ferrara, Ferrara, Italy

¹⁸ Sezione INFN di Firenze, Firenze, Italy

¹⁹ Laboratori Nazionali dell’INFN di Frascati, Frascati, Italy

²⁰ Sezione INFN di Genova, Genova, Italy

²¹ Sezione INFN di Milano Bicocca, Milano, Italy

²² Sezione INFN di Milano, Milano, Italy

- ²³ *Sezione INFN di Padova, Padova, Italy*
- ²⁴ *Sezione INFN di Pisa, Pisa, Italy*
- ²⁵ *Sezione INFN di Roma Tor Vergata, Roma, Italy*
- ²⁶ *Sezione INFN di Roma La Sapienza, Roma, Italy*
- ²⁷ *Henryk Niewodniczanski Institute of Nuclear Physics Polish Academy of Sciences, Kraków, Poland*
- ²⁸ *AGH - University of Science and Technology, Faculty of Physics and Applied Computer Science, Kraków, Poland*
- ²⁹ *National Center for Nuclear Research (NCBJ), Warsaw, Poland*
- ³⁰ *Horia Hulubei National Institute of Physics and Nuclear Engineering, Bucharest-Magurele, Romania*
- ³¹ *Petersburg Nuclear Physics Institute (PNPI), Gatchina, Russia*
- ³² *Institute of Theoretical and Experimental Physics (ITEP), Moscow, Russia*
- ³³ *Institute of Nuclear Physics, Moscow State University (SINP MSU), Moscow, Russia*
- ³⁴ *Institute for Nuclear Research of the Russian Academy of Sciences (INR RAN), Moscow, Russia*
- ³⁵ *Yandex School of Data Analysis, Moscow, Russia*
- ³⁶ *Budker Institute of Nuclear Physics (SB RAS) and Novosibirsk State University, Novosibirsk, Russia*
- ³⁷ *Institute for High Energy Physics (IHEP), Protvino, Russia*
- ³⁸ *ICCUB, Universitat de Barcelona, Barcelona, Spain*
- ³⁹ *Universidad de Santiago de Compostela, Santiago de Compostela, Spain*
- ⁴⁰ *European Organization for Nuclear Research (CERN), Geneva, Switzerland*
- ⁴¹ *Ecole Polytechnique Fédérale de Lausanne (EPFL), Lausanne, Switzerland*
- ⁴² *Physik-Institut, Universität Zürich, Zürich, Switzerland*
- ⁴³ *Nikhef National Institute for Subatomic Physics, Amsterdam, The Netherlands*
- ⁴⁴ *Nikhef National Institute for Subatomic Physics and VU University Amsterdam, Amsterdam, The Netherlands*
- ⁴⁵ *NSC Kharkiv Institute of Physics and Technology (NSC KIPT), Kharkiv, Ukraine*
- ⁴⁶ *Institute for Nuclear Research of the National Academy of Sciences (KINR), Kyiv, Ukraine*
- ⁴⁷ *University of Birmingham, Birmingham, United Kingdom*
- ⁴⁸ *H.H. Wills Physics Laboratory, University of Bristol, Bristol, United Kingdom*
- ⁴⁹ *Cavendish Laboratory, University of Cambridge, Cambridge, United Kingdom*
- ⁵⁰ *Department of Physics, University of Warwick, Coventry, United Kingdom*
- ⁵¹ *STFC Rutherford Appleton Laboratory, Didcot, United Kingdom*
- ⁵² *School of Physics and Astronomy, University of Edinburgh, Edinburgh, United Kingdom*
- ⁵³ *School of Physics and Astronomy, University of Glasgow, Glasgow, United Kingdom*
- ⁵⁴ *Oliver Lodge Laboratory, University of Liverpool, Liverpool, United Kingdom*
- ⁵⁵ *Imperial College London, London, United Kingdom*
- ⁵⁶ *School of Physics and Astronomy, University of Manchester, Manchester, United Kingdom*
- ⁵⁷ *Department of Physics, University of Oxford, Oxford, United Kingdom*
- ⁵⁸ *Massachusetts Institute of Technology, Cambridge, MA, United States*
- ⁵⁹ *University of Cincinnati, Cincinnati, OH, United States*
- ⁶⁰ *University of Maryland, College Park, MD, United States*
- ⁶¹ *Syracuse University, Syracuse, NY, United States*
- ⁶² *Pontifícia Universidade Católica do Rio de Janeiro (PUC-Rio), Rio de Janeiro, Brazil, associated to ²*
- ⁶³ *University of Chinese Academy of Sciences, Beijing, China, associated to ³*
- ⁶⁴ *Institute of Particle Physics, Central China Normal University, Wuhan, Hubei, China, associated to ³*
- ⁶⁵ *Departamento de Física, Universidad Nacional de Colombia, Bogota, Colombia, associated to ⁸*
- ⁶⁶ *Institut für Physik, Universität Rostock, Rostock, Germany, associated to ¹²*
- ⁶⁷ *National Research Centre Kurchatov Institute, Moscow, Russia, associated to ³²*
- ⁶⁸ *Instituto de Física Corpuscular (IFIC), Universitat de Valencia-CSIC, Valencia, Spain, associated to ³⁸*
- ⁶⁹ *Van Swinderen Institute, University of Groningen, Groningen, The Netherlands, associated to ⁴³*
- ^a *Universidade Federal do Triângulo Mineiro (UFTM), Uberaba-MG, Brazil*
- ^b *Laboratoire Leprince-Ringuet, Palaiseau, France*
- ^c *P.N. Lebedev Physical Institute, Russian Academy of Science (LPI RAS), Moscow, Russia*
- ^d *Università di Bari, Bari, Italy*
- ^e *Università di Bologna, Bologna, Italy*
- ^f *Università di Cagliari, Cagliari, Italy*
- ^g *Università di Ferrara, Ferrara, Italy*

- ^h *Università di Genova, Genova, Italy*
- ⁱ *Università di Milano Bicocca, Milano, Italy*
- ^j *Università di Roma Tor Vergata, Roma, Italy*
- ^k *Università di Roma La Sapienza, Roma, Italy*
- ^l *AGH - University of Science and Technology, Faculty of Computer Science, Electronics and Telecommunications, Kraków, Poland*
- ^m *LIFAEELS, La Salle, Universitat Ramon Llull, Barcelona, Spain*
- ⁿ *Hanoi University of Science, Hanoi, Viet Nam*
- ^o *Università di Padova, Padova, Italy*
- ^p *Università di Pisa, Pisa, Italy*
- ^q *Università degli Studi di Milano, Milano, Italy*
- ^r *Università di Urbino, Urbino, Italy*
- ^s *Università della Basilicata, Potenza, Italy*
- ^t *Scuola Normale Superiore, Pisa, Italy*
- ^u *Università di Modena e Reggio Emilia, Modena, Italy*
- ^v *Iligan Institute of Technology (IIT), Iligan, Philippines*